Quantifying flow in variably wet microporous carbonates using object-based geological modelling and both lattice-Boltzmann and pore network fluid flow simulations

AAPG BULLETIN

Quantifying flow in variably wet microporous carbonates using object-based geological modelling and both lattice-Boltzmann and pore network fluid flow simulations

S. R. Harland, R. A. Wood, A. Curtis, M. I. J. van Dijke, K. Stratford, Z. Jiang, W. Kallel, and K. Sorbie

AAPG Bulletin published online 06 August 2015
doi: 10.1306/04231514122

Cite as: Harland, S. R., R. A. Wood, A. Curtis, M. I. J. van Dijke, K. Stratford, Z. Jiang, W. Kallel, and K. Sorbie, Quantifying flow in variably wet microporous carbonates using object-based geological modelling and both lattice-Boltzmann and pore network fluid flow simulations, *(in press; preliminary version published online Ahead of Print* 06 August 2015*):* AAPG Bulletin, doi: 10.1306/04231514122.

Quantifying flow in variably wet microporous carbonates using object-based geological modelling and both lattice-Boltzmann and pore network fluid flow simulations

Harland. S.R.[1], Wood. R.A.[1], Curtis. A.[1], van Dijke. M.I.J.[2], Stratford. K.[3], Jiang. Z.[2], Kallel. W.[2], Sorbie. K.[2]

[1]School of GeoSciences, University of Edinburgh, West Mains Road, Edinburgh, EH9 3JW

[2]Institute of Petroleum Engineering, Heriot-Watt University, Riccarton, EH14 4AS

[3]EPCC, University of Edinburgh, JCMB, Mayfield Road, Edinburgh, EH9 3JZ

Acknowledgements

The authors are grateful to the sponsors of this Industry Technology Facilitator (ITF) project BG Group, Chevron, Dong Energy and Wintershall for funding and for permission to publish this work. We thank the Edinburgh Parallel Computing Centre (EPCC) for allowing access to the BGQ machine and computational time. Kevin Stratford acknowledges support from UK EPSRC grant EP/J007404.

ABSTRACT

Micropores can constitute up to 100% of the total porosity within carbonate hosted hydrocarbon reservoirs, usually existing within micritic fabrics. Here, 3D computational representations of end-point micritic fabrics are produced using a flexible, object-based algorithm to further our understanding of the contribution that micropores make to flow. By methodically altering model parameters we explore the state-space of microporous carbonates, quantifying single- and multi-phase flow using lattice-Boltzmann and network

models.

In purely micritic fabrics, average pore radius (ranging from 0.26μm to 0.44μm) was found to have a positive correlation with single-phase permeability (1.7md to 2.7md respectively). Similarly, increasing average pore size resulted in decreasing residual oil saturation under both water-wet and 50% fractionally oil-wet states. Similarly, permeability was found to increase by an order of magnitude (from 0.6md to 7.5md) within fabrics of varying total matrix porosity (from 18% to 35%) due to increasing pore size (0.37μm to 0.56μm respectively), but minimal effect on multi-phase flow was observed. Increased pore size due to micrite rounding notably increases permeability in comparison to original rhombic fabrics with the same porosity but multi-phase flow properties are unaffected.

Finally, when moldic mesopores are added to a micritic matrix, they impact flow when directly connected. Otherwise, micropores control single-phase permeability magnitude. Importantly, recovery is dependent on both wetting scenario and pore-network homogeneity: under water-wet imbibition, increasing proportions of microporosity yield lower residual oil saturations.

Together, these results quantify the importance of micropores in contributing to, or controlling, overall flow and sweep characteristics in such fabrics.

INTRODUCTION

Carbonate Micropores

Understanding the pore system and petrophysical properties of reservoir rocks is vital for accurate prediction of fluid flow behaviour and therefore hydrocarbon recovery. Predicting such properties for carbonate rocks can be a particularly complex task as their pore systems are inherently multi-scale, often spanning four relevant orders of magnitude of pore size variation (Choquette and Pray, 1970). Perhaps the least understood type of pore space

within carbonates is micropores. There are many definitions for micropores, including pores <10μm in diameter and hence below the resolution of an optical microscope (Anselmetti et al., 1998; Cantrell and Hagerty, 1999; definition applied to this study), or pores less than 62.5μm in diameter (Choquette and Pray, 1970), or pores less than 1μm in diameter in at least one direction (Pittman, 1971).

Carbonate micropores have many origins (Pittman, 1971; Moshier, 1989a; Budd, 1989), but the most pervasive form is found between the crystal faces of rhombic micrite (micro-crystalline calcite, Figure 1a; see Folk, 1962), often termed chalky micropores. The formation of these micropores is not fully understood, but may occur through the transformation of acicular high-magnesium calcite and aragonite lime mud crystals into micro-rhombic low-magnesium calcite (Moshier, 1989a) via precipitation, dissolution and recrystallization, although the exact details of the process are still debated (Dravis, 1989; Cantrell and Hagerty, 1999; Heasley et al., 2000; Lambert et al., 2006; Volery et al., 2009; Lucia and Loucks, 2013). Such micropores have a distinct 'plate-like' morphology (Cantrell and Hagerty, 1999) and one spatial dimension maybe up to an order of magnitude smaller than the other two dimensions. In the smallest dimension the pores are 0.1μm while in the other two dimensions they are around 1μm (as observed in the inset of Figure 1b and reported by Cantrell and Hagerty (1999) from similar images). Nevertheless, such pores may constitute a significant percentage of the total porosity and potential storage capacity (up to 100% in mud dominated facies) of some of the largest known carbonate reservoirs, for example the Middle Eastern Upper Jurassic Arab Formation (Cantrell and Hagerty, 1999; Clerke et al., 2008; Clerke, 2009; Lambert et al., 2006) and the Lower Cretaceous Thamama group (Moshier, 1989b; Budd, 1989; Smith et al., 2003; Lambert et al., 2006; Cox et al., 2010; Deville de Periere, 2011; Fullmer et al., 2014).

Such microporous carbonates have different rock fabric properties which can vary

throughout a reservoir and micropores occur in both mono-modal and multi-modal pore systems that can incorporate mesopores, macropores and fractures or fissures (e.g. Cantrell and Hagerty, 1999; Clerke et al., 2008). Micropore morphology (size and shape) is controlled by the different shapes, styles of packing and size distribution of the micrite crystals, which have been classified under various schemes by a few different studies (Lambert et al., 2006; Volery et al., 2010; Deville de Periere et al., 2011; Fullmer et al., 2014). Micropores can be found within micritised grains, or as pervasive horizons of micritic matrix (with or without larger mesopores), or between grains where the inter-granular pore space has been micritised (Cantrell and Hagerty, 1999; Clerke et al., 2008). An additional feature of some microporous carbonates, particularly those in the Middle East, is rounded micrite (Budd, 1989; Moshier, 1989b; Wagner, 1990) which is typically found towards the top of the oil column and reported to have better reservoir properties (high porosity and single-phase permeability) than their rhombic counterparts (Lambert et al., 2006). A possible explanation for these fabrics is that acidic fluids flowing through the micropore network prior to hydrocarbon emplacement, dissolve the edges and vertices of the rhombic micrite crystals to leave rounded crystals with a reduced crystal size (see Figure 1c and Lambert et al., 2006), although this process is still debated (Ehrenberg et al., 2012).

Current Understanding of Flow Through Micropores

It is often assumed that hydrocarbons were unlikely to be emplaced into micropores during primary drainage (due to the small pore throat diameters, typically <1μm, and resultant high capillary pressure), and that micropores therefore contributed very little to fluid flow through the reservoir unit, containing only bound, irreducible waters (Pittman, 1971; Kirkham et al., 1996). However, hydrocarbons have long been observed to exist within micropores, with increasing oil saturations towards the top of the oil column (Al-Yousef et al., 1995; Lambert et al., 2006; Fung et al., 2011; Clerke et al., 2014). Petrophysical studies focusing on the

core-scale to large-scale flow properties of microporous carbonate reservoirs, use both modelling and experimental methods to quantity flow, with a large number of in-depth studies published on the Arab D member (e.g. Sallier and Hamon, 2005; Masalmeh and Jing, 2007; Clerke et al., 2008; Funk and Al-Harbi, 2009; Fung et al., 2011; Clerke et al., 2014). Initial recovery from microporous dual porosity systems (often fractured or fissured reservoirs) is typically very low as hydrocarbons within the micropores are often not recoverable during primary production (observed in limestones, chalks and sandstones). However, many studies, dating back to the 1950's have shown that under strongly water wet scenarios forced imbibition methods can be used to extract remaining oil reserves from the micropores in these fractured/fissured reservoirs, re-establishing their importance during production (see for example Barenblatt et al., 2003 and references therein).

More recently, pore-network models and pore scale studies have been used to examine the effects of micropores on flow. While micropore-dominated carbonates have typically low permeabilities (less than 10md), the pervasive distribution of micropores has been shown to result in a higher sweep efficiency within intervals with a high percentage of micropores (Wu et al., 2008; Clerke et al., 2009; Hollis et al., 2010; Clerke et al., 2013; Fullmer et al., 2014). Additionally, it has been shown that within some multi-scale pore networks, micropores provide the connectivity and fluid pathway between otherwise disconnected larger scales of pores (Figure 1b). For example, Roth et al (2011) demonstrated that connectivity through a multi-scale carbonate pore network was only achieved when pores <12μm in diameter were present in the model. In these models, micropores actually controlled the percolation threshold. Few studies have however attempted to compare the petrophysical properties of the various microporous, micrite dominated fabrics in order to understand their different flow properties, and particularly the different multi-phase flow properties.

123 **Pore Scale Rock Modelling Methodologies**

124 To understand the flow properties of micropores, direct 3D imaging of the rock using
125 methods such as computer tomography or focussed ion beams (FIBSEM) would be ideal.
126 Micropores are below the typical standard micro-computed tomography (CT) resolution of a
127 couple of microns, requiring high resolution nano-CT or FIBSEM technologies (resolution
128 <100nm). A large number of studies have successfully utilised these technologies to
129 characterise the pore space of carbonates and to examine flow properties of extracted pore
130 networks (see Van Geet et al (2000), Cnudde and Boone (2013) and Blunt et al (2013) for
131 overviews and references therein). However, these methods are expensive, with FIBSEM
132 also being destructive, and resultant sample volumes are typically small (<15μm^3) due to
133 the trade-off between resolution and image volume. They also provide limited flexibility to
134 study the effect of variations in rock fabric properties as the properties of the image cannot
135 be adjusted with ease, if at all. Micro-model methods, such as those used by Buchgraber et
136 al (2012), are similarly useful for imaging multi-phase fluid interactions but have a limited
137 application to 3D flow properties. As such, to further examine the effect of variations in
138 microporous fabric properties, both individually and in combination, on flow properties,
139 digital rock reconstruction methods that focus on reproducing geological fabrics to infer the
140 pore-space, provide a more viable and flexible methodology. Indeed, the pore network of a
141 rock is created by its fabric, so by accurately reconstructing the solid phase(s), the pore
142 network and therefore the petrophysical flow characteristics (e.g. porosity, absolute
143 permeability, relative permeability and capillary pressure curves) of the medium can be
144 determined.

145 Many different methodologies have been developed to produce digital 3D models of porous
146 media (see in-depth overview by Blunt et al., 2013). For example, there are object-based
147 modelling methods, including process-based reconstructions (e.g. Bakke and Øren, 1997;

148 Øren and Bakke, 2003) and continuum based reconstructions (e.g. Biswal et al., 2007;
149 2009a,b), and there are statistical or stochastic reconstructions from 2D images (e.g.
150 Okabe and Blunt, 2004; Al-Kharusi and Blunt, 2008; Wu et al., 2004, 2006; 2008).

151 While all proposed methods provide advantages for certain applications, they have
152 limitations for modelling micropores. For example, reconstructions based on the spatial
153 statistics of 2D images can be used to create 3D models using multipoint-statistic
154 techniques (Okabe and Blunt, 2004; Al-Kharusi and Blunt, 2008) or stochastic approaches
155 involving Markov meshes (Wu et al., 2004, 2006; 2008). These statistical approaches,
156 however, tend to smooth the true variations in the image structure, and as such fail to
157 capture the heterogeneous nature of multi-scale pore systems such as those within
158 carbonates, however methods have been developed to combine both low resolution and
159 high resolution data types (e.g. Hurley et al., 2011). Object-based models provide perhaps
160 the most flexible basis for modelling rock fabrics as the properties can be altered and
161 adjusted to recreate all geological variability based on observations. However, the complex
162 processes of carbonate diagenesis mean that process-based modelling methodologies,
163 which work very well for reconstructing sandstones (Bakke and Øren, 1997; Øren and
164 Bakke, 2003), are problematic to implement for carbonates. The primary and diagenetic
165 processes of micrite formation are not only poorly understood, but may also vary from
166 reservoir to reservoir (Budd, 1989; Moshier, 1989a; Moshier, 1989b; Cantrell and Hagerty,
167 1999; Lambert et al., 2006; Richard et al., 2007; Volery et al., 2009; Lucia and Loucks,
168 2013). Continuum based modelling methodologies (e.g. Biswal et al., 2007; 2009a,b)
169 provide a unique approach which combines low resolution micro-CT scans with 2D
170 geological and crystal information in a continuum object-based technique to reproduce
171 carbonate fabrics at multiple resolutions. While the method of incorporating multiple fabrics
172 and pore types into a model is an advanced technique, in order to simulate flow, the

continuum model has to be discretised at a specific resolution. Models at adequate resolutions to model micropores within carbonate fabrics have been generated using such continuum methods (Roth et al., 2011), but these were not used to quantify the petrophysical or multi-phase properties of the microporous fabrics.

Overview

In this study, we present an object-based digital rock building methodology that aims to accurately reconstruct the end-point micro-scale micritic fabrics of microporous carbonates in order to accurately capture the relevant statistical properties of the pore space. Both quantitative and qualitative underlying data are used to populate the models based on data from 2D SEM image analysis of samples from the Early Cretaceous Thamama Group, Arabian Gulf; a shallow ramp marine carbonate. The algorithm is flexible such that it can model the textural variations of microporous carbonates and include multiple scales of pores. This new methodology is thus able to reconstruct reservoir rocks at a resolution suitable for capturing micropores, enabling interrogation of both single-phase and multi-phase flow in such microporous carbonates.

In what follows, we use the algorithm in combination with a lattice-Boltzmann simulator, a pore network extraction algorithm and a network model multi-phase phase flow simulator to study the single- and multi-phase flow properties of synthetically generated typical Middle Eastern microporous carbonates. In particular, we focus on micrite dominated fabrics and consider the effect of micropore size, total micropore content and the effect of micritic dissolution within models of purely micritic matrix. Finally, we examine how moldic mesopores within a microporous matrix affect flow properties.

METHODOLOGY

Textural Properties of Micrite and Micropores

197 The 3D model needs to be calibrated with geostatistical data. Since it is difficult to image
198 micropores directly using 3D scanning methods, following other studies (Biswal et al., 2007,
199 2009a, 2009b; Deville de Periere et al., 2011) we use scanning electron microscope (SEM)
200 images to capture the basic textural properties of microporous carbonates. Image analysis
201 is performed using IMAGEJ (Schneider et al., 2012).

202 Different SEM imaging methods are used to extract both quantitative and qualitative data to
203 calibrate the models. Secondary electron images provide a shallow, pseudo-3D image of
204 broken chips (Figure 1a,c) which allows the crystal form and the nature of the contact
205 between crystals to be examined. For example, the micrite in the microporous sample in
206 Figure 1a consists of approximately equidimensional sub-rounded to euhedral rhomboids,
207 often with multiple facets, and there is no obvious alignment of crystal orientation.

208 Images of epoxy resin pore casts (Figure 1b) are used provide insight into the form, size
209 and distribution of different pore types (mesopore and micropore) within a sample. They
210 also provide crucial information about the nature of 3D connectivity between pores. For
211 example, the highly connected sponge-like network of micropores, and the connectivity
212 between this network and a mesopore, can be seen in Figure 1b. Produced using low
213 pressures, the epoxy resin cast was validated against rock chips by comparing crystal
214 dimensions in the cast to crystal dimensions in the rock chips to ensure that the sample had
215 not been altered during preparation.

216 Finally, backscatter images of highly polished, flat sample surfaces (Figure 2a,b) provide a
217 good contrast between pore and solid. They enable easy binarisation to determine 2D slice
218 porosities and also allow measurements of crystal diameter to be made within the image
219 plane. SEM images are taken at a very high resolution (here up to 0.05μm/pixel) and as
220 such, before any crystal diameter data are extracted through image analysis, the resolution
221 of the SEM image needs to be reduced (by averaging across neighbouring pixels) to match

222 that of the models which will be generated, removing features that would be unresolvable at
223 the model resolution. Subsequently, a watershed algorithm can be applied to detect
224 individual crystals and Feret diameter measurements (with amalgamated crystals removed)
225 can be made to provide a quantitative crystal size distribution (CSD, Figure 2c) from which
226 the model can be populated. Where it is not possible to detect crystal edges through an
227 automated process, manual measurements of the longest diagonal length of the crystal can
228 be made instead. The resulting data are 2D crystal diameters, ranging from the image
229 resolution up to 4μm (Figure 2c), similar to that reported by Deville de Periere et al (2011).
230 In addition to cross-correlation with data in the literature, the CSD was cross-correlated
231 against measurements performed on secondary electron images in this study. By collecting
232 a statistically significant number of diameters (here, over 400 measurements) the measured
233 CSD data are assumed to be reflective to the 3D crystal diameters.

234 **Object-Based Reconstruction Methodology**

235 The crystal size distribution (Figure 2c) is used to build a library of 3D micrite crystals at the
236 model resolution, including forms rotated around the x, y and z axes at discrete intervals
237 throughout the desired range of rotations. Micrite crystals have multiple facets and are often
238 observed to be sub-rounded to a degree. In order to capture these properties precisely, an
239 unrealistically high resolution digital model would be required. As such the rhombs are
240 simplified to cubes; this approximation maintains the approximately equidimensional and
241 euhedral nature of micrite, but reduces the voxel resolution required to represent the crystal
242 form, acting as an end-point fabric. However, the algorithm is flexible such that if multiple
243 crystal types, shapes and sizes were required, these could simply be included in the library.

244 When distributing the crystals, matrix connectivity is guaranteed by allowing (or forcing) an
245 overlap of neighbouring crystals. Crystals in the library have a layered structure where
246 voxels on the edges of the crystal are identified; these are allowed to overlap with other

crystal edge voxels, while crystal centers must remain non-overlapping (Figure 3a,b). This technique has similarities to the 'cherry-pit' or penetrable-concentric-shell (PCS) model (Torquato 1984, 1985, 1986). As such, the smallest crystal size for any model resolution is 3^3 voxels to ensure a distinction between crystal centers and crystal edge voxels exists (Figure 3c,d). The degree of overlap can be varied, allowing different styles of micrite packing to be represented, but a minimum edge layer thickness of one voxel is required at any resolution to maintain matrix connectivity.

The rock reconstruction is initialised within a 3D space, discretised into a grid of regular cubic voxels of a predefined physical size (the resolution). In an iterative process, voxels are defined as solid by randomly fitting micrite crystals from the library into the grid. This continues until a desired total percentage of solid, and therefore the desired total porosity (ϕ_D) is achieved. Crystals are fitted from largest to smallest, with the number of iterations ($\mathrm{N_i^C}$) of each crystal size (indexed by i) calculated based on the known crystal frequency distribution (f_i^C, as shown for example in Figure 2c), the volume of each crystal size (V_i^C), the total volume of the grid being filled (V), and the total porosity (ϕ) required in the final model which is related to ϕ_D as described below. As such the number of iterations of each crystal size required to achieve the target porosity is predetermined based on the ratio (R) between the volume of solid produced by the crystal size distribution and the volume of the model to be created as shown in Equations (1) and (2):

$$R = \frac{V}{(1-\phi)\times\sum_{i=1}^{n} V_i^C \times f_i^C} \quad (1)$$

$$N_i^C = R \times f_i^C \quad (2)$$

The overlapping edge voxels of the crystals result in an underestimate of the number of crystals required to fill the volume as overlapping edges are not accounted for in Equations

269 (1) and (2), hence the resulting final porosity would always be higher than the required
270 porosity. To account for this, the target porosity (ϕ in Equations (1) and (2)) is set at a value
271 that is predictably lower than the desired porosity (ϕ_D). This prediction is based upon a
272 sensitivity test to determine the average loss in solid voxels due to overlap at a desired
273 porosity. An example is shown in Figure 4.

274 At each iteration during model generation, a random (possibly rotated) crystal of the correct
275 dimensions is selected from the crystal library. Randomly selected potential grid locations
276 are successively tested until a location that satisfies the edge and centre placement
277 conditions is found. Upon completion, the algorithm results in a binary model (Figure 3b) of
278 the foreordained porosity (ϕ_D) that is 100% microporous and a solid proportion that is 100%
279 micrite. Data specific to each crystal placed into the model (such as crystal centre
280 coordinates, crystal diameter and rotation information) are stored in an array as objects are
281 placed into the volume. This information may be used to manipulate the model fabrics to
282 perform rounding of the micrite crystals to emulate micritic dissolution, or to include larger
283 scale features such as mesopores (pores >10μm in diameter). The properties of mesopores
284 can be determined from the SEM images in a similar manner to the properties of micrite.

285 Micrite rounding is performed homogeneously across the model volume. The cubic form of
286 the micrite crystals is altered to a spherical form by tracing the inscribed radius of the
287 crystals based on their diameter. Because of the alteration to the fabric it is again important
288 to ensure matrix connectivity of the rounded crystals. This is achieved by testing that each
289 crystal touches at least one other. If this is not satisfied, slight shifts of the unconnected
290 crystals are made to abut them against another crystal. In the highest porosity models
291 generated for this study, this shift process affected less 0.4% of the crystals, but must
292 nevertheless be performed to reflect the rock texture and avoid floating crystals in the
293 matrix.

The purely microporous models can subsequently be merged, under certain conditions, with larger scale pores to generate multi-scale networks. The mesopore networks can be derived from subsections of micro-CT images or can be synthetically generated to represent, for example, moldic mesopores (Figure 1b). The modelled moldic mesopores here are simplified to spherical bodies, although more complex shapes can be used. The size and location of the molds within the modelled volume can be determined randomly or predefined.

Although this process of merging the two pore systems does not reflect the processes of formation of the mesopores and the micritic matrix, the fabrics generated do reflect those observed from SEM analysis such as the connectivity between mesopores and microporosity (Figure 1b) and the rugosity around mesopore edges due to micrite crystals (Figure 2b).

Sensitivity Analysis of Fluid Flow Properties to End-Point Rock Fabric Properties

Here in we begin to explore the variability of micritic microporous carbonate rocks to investigate the flow properties of different end-point fabrics. First, we investigate the sensitivity of flow properties to micropore size, controlled by varying the resolution at which each model is generated. Micropore size is likely to vary from reservoir to reservoir and also within any individual reservoir. Models were generated at five different resolutions: 0.50μm^3/voxel, 0.40μm^3/voxel, 0.30μm^3/voxel, 0.20μm^3/voxel and 0.10μm^3/voxel (models r_5 to r_1 respectively), with three realisations generated at each resolution. Each model had a porosity of approximately 26% and a volume of 400^3 (64 million), the physical size therefore varied between models (Table 1). Both single- and multi-phase flow were simulated on the models, however in order to be able to compare the single-phase properties of the different fabrics properly, eight subvolumes of the four lowest resolution models (r_2 to r_5) were also

319 isolated. These subvolumes each had the same physical volume ($40^3\mu m^3$) as the highest
320 resolution model (r_1). The computational sizes of these subvolume models are shown in
321 Table 1.

322 Secondly, we consider the effect of total porosity on fluid flow within a purely micritic fabric
323 and also investigate the effect of micrite rounding. Total porosity was varied from 18% to
324 35% (models r_a to r_e respectively) and three realisations of each model were created. These
325 porosities are within the range of reported values for purely microporous carbonates
326 (Cantrell and Hagerty, 1999; Clerke et al., 2008; Volery et al., 2010; Deville de Periere et
327 al., 2011; Clerke et al., 2013; Fullmer et al., 2014) and of porosities from SEM image
328 analysis performed for this study. These models were created at a resolution of
329 $0.40\mu m^3$/voxel and were again 400 voxels (or 160μm) in length. Micrite rounding was
330 performed on one model at each given porosity (models s_a to s_e) to investigate its effect on
331 flow.

332 Finally, we investigate the effect of synthetic spherical moldic mesopores (pore
333 diameter >10μm) within a micritic matrix of varying total (micro- and meso-) porosity.
334 Although fully microporous horizons do exist within reservoirs, it is additionally important to
335 understand the range of multi-scale fabrics in which micropores do (and do not) contribute
336 to flow. A mesopore was placed in each octant of a $400voxel^3$ model generated at a
337 resolution of $0.40\mu m^3$/voxel. Amongst other properties, mesopore size varies and as such,
338 the radii of the mesopores in the models varied between 10μm and 45μm, generating five
339 different model fabrics. These mesopore models were combined with purely micritic
340 matrices, with total matrix porosities of 18%, 25% and 35%.

341 All models generated during this study used a crystal size distribution measured from SEM
342 image analysis of samples (Figure 2c), discretised to the correct resolution in order to
343 create appropriate corresponding crystal libraries.

Simulation of flow

Two separate methodologies are employed to simulate single- and multi-phase flow in this study. We describe each in turn.

Single-phase Flow Simulation

Single-phase flow simulation for the computation of absolute permeability is performed directly on the discretised model using a multiple relaxation time (MRT: Chun and Ladd, 2007) lattice-Boltzmann model (Ludwig: Desplat et al., 2001) which represents the boundaries of solid objects using a simple bounce-back scheme. Simulations are performed in lattice units (lu), and converted to millidarcys (md) based on the true voxel size (Δx). A permeability is obtained by computing the steady-state volume flux in a periodic system (obtained by reflecting the volume along the flow direction and using periodic boundaries) generated by a constant body force with a viscosity (η) of 1/6 in all cases. The simulations were parallelised and used 2048 cores on the Blue Gene/Q supercomputer based at the Edinburgh Parallel Computing Centre.

The steady state volume flux (Q) is related to the macro-scale permeability (k) by the Darcy equation (Equation (3) below, Darcy, 1856) where the differential pressure ($\mathrm{P_b} - \mathrm{P_a}$) is related to the applied body force and the length of the system in the flow direction (L) of cross-sectional area (A) by

$$Q = -\frac{kA}{\eta}\frac{(P_b - P_a)}{L} \qquad (3)$$

As is usual with this type of calculation, we ensure that the final pore-scale Reynolds number is below unity to simulate incompressible Newtonian, laminar flow. For the narrowest pores in the system, we would expect the flow to be poorly resolved which would lead to some systematic, and likely, underestimates in the permeability. Tests in capillaries with regular geometries (circular, triangular, square cross-section) suggest errors in

computed permeability to be up to ≈25% for widths less than ~4Δx (Sengupta et al., 2012).

Multi-phase Flow Simulation

We perform multi-phase flow simulations on pore networks extracted from the generated models using the Pore Architecture Tool (PAT) algorithm developed by Jiang et al (2007). This method is based on extracting the local medial axis through the pore space (using a thinning algorithm) and separating the network into pore bodies and throats (nodes and bonds respectively), preserving the connectivity and topological characteristics of the pore space. Junctions in the network are defined as pore bodies (nodes) and the connecting pathways between nodes are then throats (bonds). Quantitative geometrical characteristics of the network elements such as pore radius, perimeter, and area and shape factor are all determined. These geometrical properties control the development and stability of wetting layers within the network elements (Blunt, 1998; Valvatne and Blunt, 2004). The topology (or connectivity) of the pore network plays an important role in controlling multi-phase flow properties and can be described in two ways. Firstly it can be described through the coordination number; the number of bonds connecting to each node in the network. And/or secondly it can be described by calculating the specific Euler number (χ, Vogel and Roth, 2001) which is simply the number of nodes (N) minus the number of bonds (B) divided by the volume of the model (V):

$$\chi = \frac{N-B}{V} \qquad (4)$$

The Euler number can also be used to derive the pore size dependent connectivity function by removing pores from the network in order of increasing size and recalculating the Euler number at each step (Vogel and Roth, 2001). Removing larger and larger pores will eventually result in a positive Euler number (fewer bonds than nodes) which indicates the point at which the network becomes unconnected. As such an Euler number of zero is a

proxy for the percolation radius of the network.

Multi-phase flow was simulated on the extracted networks using the quasi-static (capillary dominated flow) Poreflow software (Valvatne and Blunt, 2004). Two-phase flow is simulated according to invasion-percolation principles during drainage (invasion of oil) and imbibition (invasion of water). A pressure gradient is applied to each phase across the pore network (between the inlet and outlet face) and the relative permeabilities of each phase are determined by calculating the pressure distribution in response to the change in pressure gradient across each phase at each node, using mass conservation (Øren et al., 1998). Note that the assumption of dominance of capillary over viscous forces, which is justified for the considered small pore sizes, implies that the relative permeabilities do not vary with fluid viscosities.

In order to simulate multi-phase flow, the pore-scale wetting properties of the model must be predefined. However, the wetting properties of carbonates and specifically micropores are poorly understood. Strong variations of wettability in different reservoirs are observed more frequently in carbonate reservoirs than in siliciclastic reservoirs (Bobek et al., 1958) and studies into the wettability of globally distributed carbonates (e.g. Treiber and Owens, 1972; Kashfi, 1974; Morrow, 1976; Chilingar and Yen, 1983; Cuiec, 1984) have indeed produced varying results. Some carbonates have, however, been found to have a more definite mixed wetting state (Lichaa et al., 1993; Al-Yousef et al., 1995; Okasha et al., 2001; Skauge et al., 2004, 2006, 2007; Okasha et al., 2007; Knackstedt et al., 2011) with small pores having a weak affinity towards oil (Skauge et al., 2006; Marathe et al. 2012; Dodd et al., 2014). Estimating wettability at the core plug scale is a complex task in itself and few studies have been able to examine the wettability distribution at the pore scale, although recent Field-Emission SEM studies have shown advances toward achieving this (Marathe et al. 2012; Dodd et al., 2014). Here, two different imbibition (water flood) wettability

scenarios at the pore scale were simulated to characterise concomitant variations in the multi-phase flow properties. For both scenarios, the pore network is initially assumed to be strongly water-wet and oil flooding (water drainage) continues until a minimum residual water saturation of 0.07 has been achieved. For the first imbibition scenario, the rock remains water wet (WW) after drainage and no aging occurs. For the second imbibition scenario, the rock is fractionally wet (FW), where after drainage, 50% of the pores become oil-wet (due to aging). This type of wettability distribution is neither pore shape nor pore size dependent, thus making the fewest assumptions in the absence of reservoir core data. For both wettability scenarios, imbibition continues until a minimum residual oil is achieved.

RESULTS

Effect of Micropore Size

Model Fabric Properties

The morphology of the micritic fabrics in the models matches well with that which is observed in SEM images under the assumptions and simplifications of the algorithm (Figure 5). In particular, the models show similar crystal packing and distributions to those observed in samples (Figure 5c,d). Crystal morphology in samples is typically of a more sub-rounded form (Figure 5a) than those in the model (Figure 5b) due to the resolution limitations of the modelling method, as discussed previously.

Figure 6 shows 2D slices through a 3D realisation at each resolution, scaled relative to their physical sizes. Visually the models can be seen to be producing very similar micritic fabrics, and all have porosities of approximately 26%. The differences between the models are compounded by the pores and crystals being represented by an ever increasing number of voxels as resolution is increased from 0.50μm^3/voxel up to 0.10μm^3/voxel (subfigures a to e respectively in Figure 6). The size of the smallest resolvable feature decreases with each

increase in resolution (e.g. minimum crystal size, Table 2) while the maximum crystal size remains constant as all models use the same measured crystals size range.

Pore Network Properties

The pore radii distributions shown in Figure 7a indicate the change in pore geometry with model resolution. The box in Figure 7a shows the smallest pores in the generated models which are equal to the resolution of the model (half a voxel in radius). As resolution is progressively decreased from 0.10μm^3/voxel to 0.50μm^3/voxel (model r_1 to r_5), the smallest pores are lost from the models and at the other end of the scale, larger pores are incorporated. This is reflected in the increase in the average pore radius with a decrease in resolution (Table 2) and an increase in the upper limit of the pores captured by the models (Figure 7a). Average pore radius increases by nearly 70% across the different models, from 0.26μm for model r_1 up to 0.44μm for model r_5.

The percolation radius (where the Euler number is 0) can be seen to be dependent on model resolution (Figure 7b). Models r_1 to r_4 have a percolation radius of ~0.30μm while model r_5 shows a distinct increase up to a percolation radius of 0.38μm. In model r_5, the smallest connections (which control flow in the models of higher resolution) have been lost, and as such the geometry and topology of the system has been altered changing the connectivity of the pores. This change in network properties is highlighted by the decrease in the number of nodes and bonds between model r_4 and model r_5 (Table 2). Based on these observed changes in the pore network, a change in the fluid flow properties of model r_5 in comparison to the other models could be expected.

Porosity and Single-phase Permeability

All models had a target porosity of 26% and at each resolution a separate target porosity trend (Figure 4a) was generated. The resultant model porosities fluctuate randomly around

26% porosity, ranging from 26.8% porosity for model r_1 down to 25.9% porosity for model r_4 (Figure 8a). The model subvolumes (Table 1) also show a narrow range of porosities (Figure 8c) indicating that a reasonably homogeneous medium and representative elemental volume is being generated at all resolutions. The number of crystals generated in each full size model is shown in Table 2.

Single-phase permeability (Figure 8b) shows a positive correlation with average pore size. There appears to be a negative correlation between porosity and permeability (Figure 8c) contradicting expected trends in petrophysical data. This is again due to the increase in average pore size. Model r_5 has both the largest average pore radius (0.44μm) and the highest permeability, despite having a slightly lower porosity than the other models. Over the range of porosities and permeabilities shown, the variation in permeability is <1md (varying between 1.7md and 2.7md) and in porosity is <1.5% (varying between 25.5% and 27%).

Multi-phase Flow

Figure 9a-c shows the relative permeability curves from multi-phase flow simulations over the full 400^3voxel models at each resolution. These plots indicate the effective permeability of the water and oil phases against saturation. The relative permeability curves of all models are smooth indicating a homogeneous pore network has been generated at all resolutions.

Average pore size has little to no effect on water relative permeability during drainage (Figure 9a). Oil relative permeability however can be seen to increase with a decrease in average pore size at mid-range saturations. The decreasing minimum pore size in the models is reflected in the increasing maximum achieved capillary pressure from model r_5 to r_1 (Figure 9d).

Upon imbibition, a similar trend is observed. Oil relative permeability is dependent on average pore size, with individual models behaving slightly differently, while water relative permeability curves are indistinguishable under both wetting scenarios (Figure 9b,c). These variations in relative permeability result in a residual oil saturation (fractional volume of oil remaining in the model after full water flood) that is dependent on average pore size. Residual oil variation most clearly demonstrated by the capillary pressure curves in Figure 9e,f. Under both wetting states, the models show a small incremental decrease in residual oil saturation with increasing average pore size (model r_1 to r_5). Under a water wet state, residual oil decreases from 38% to 28% and under a fractionally wet state residual oil decreases from 42% to 38%, indicating the control of average pore size on multi-phase flow and particularly residual oil saturation.

Effect of Total Matrix Porosity and Micrite Rounding

Model Fabric Properties

Figure 10 shows 2D slices through a 3D realisation of each porosity model. Visually the average pore size can be seen to increase with porosity, and the models appear to represent a statistically homogeneous medium, with some random clustering of crystals as is observed in SEM images (Figure 5).

The fabric of a rhombic micrite crystal model (r_c) can be seen more clearly in Figure 11a,c which show the cubic and euhedral micrite structure. Figure 11 also shows the effect of rounding on the crystal fabric. In Figure 11b,d (showing model s_c), the original crystal structure is retained but without crystal vertices. Any apparently floating crystals are connected in the third dimension. The decrease in crystal size after micrite rounding is demonstrated in Figure 11e.

Pore Network Properties

511 Within the rhombic crystal models, average pore size increases with an increase in porosity
512 (Figure 10) which is supported by the results of the pore network extraction analysis
513 presented in Figure 12a. There is also an increase in the range of pore radii with porosity
514 although the range of pores captured in each model spans only one order of magnitude and
515 the majority of pores in the models have a radius of one voxel (two voxels in diameter,
516 Figure 12a). The homogeneity of the micritic fabric results in a narrow range of pore radii
517 reflecting a fairly homogeneous pore network. The increase in average pore size coincides
518 with an increase in the average coordination number while the total number of elements
519 decreases for the models with the highest porosities (Table 3).

520 Percolation radius increases with porosity (Figure 12b) which would be expected as the
521 average pore size increases. Models r_a, r_b and r_c have a similar percolation radius of
522 0.25μm, while models r_d and r_e show an increase to 0.35μm and 0.40μm respectively,
523 indicating that larger pores are better connected in the higher porosity models, which is
524 again reflected in the average coordination number (Table 3).

525 In comparison to their rhombic crystal counterpart, the rounded micrite models exhibit an
526 increase in the range of pore sizes present and also an increase in the average pore radius
527 (Figure 12c), due to the decrease in crystal size (Figure 11e). Individually comparing a
528 rhombic micrite model to its rounded counterpart demonstrates this trend clearly (Figure
529 12e).

530 Percolation radius increases after rounding for all models (Figure 12d,f), however the
531 average coordination number does not show a likewise increase (Table 3). The increase in
532 average coordination number after rounding in comparison to before rounding is most
533 pronounced for the low porosity models and this increase tapers off to become zero for the
534 highest porosity models which exhibit no change in average coordination number between
535 the rhombic micrite to the rounded micrite fabrics. After rounding, all models have an

536 average coordination number of greater than 4.2, whereas only rhombic models r_d and r_e
537 had average coordination numbers greater than 4.2.

538 **Porosity and Single-Phase Permeability**

539 The single-phase permeability and porosity results averaged over the individual results of
540 the three realisations for each rhombic crystal model are shown in Figure 13a,b. For each
541 set of realisations the three permeability values were within 0.01md of the mean and the
542 porosities were within 0.04% of the mean, hence the variance was negligible. Over the
543 range of modelled porosities, 18% to 35%, there is an order of magnitude variation in the
544 single-phase permeability, from 0.6md to 7.5md respectively.

545 Micrite rounding results in a porosity increase of 7-8%, and is slightly more pronounced for
546 the lowest porosity models (Figure 13b). The increase in porosity with rounding is reflected
547 in the substantial increase in single-phase permeability for each individual model as shown
548 by the dashed lines connecting the rhombic models to their rounded counterparts in (Figure
549 13b). Comparing rhombic and rounded permeability values at the same porosity (models r_d
550 and s_b), however, shows a small increase due to pore size increase through rounding.
551 Model r_d has a slightly higher porosity of 30.6% and yet an average pore radius of only
552 0.48μm while model s_b has a porosity of 29.6% and an average pore radius of 0.50μm.

553 **Multi-phase Flow**

554 Based on the pore network properties of the original rhombic crystal models (r_a to r_e), the
555 increase in average coordination number with increasing total porosity suggests that there
556 would also be a variation in the multi-phase flow properties for these models. However, this
557 expected trend is not observed (Figure 14a-c). During drainage (Figure 14a), the oil relative
558 permeability curves can be seen to depend on model porosity and therefore pore size.
559 Increasing pore size leads to a higher oil relative permeability at the same saturation, most

likely due to the presence of larger pores and due to the increase in connectivity. Water relative permeabilities are, however, almost indistinguishable, showing only a small variation between models and no discernible trend with porosity or pore size. An irreducible water saturation of 0.07 is achieved for all models.

The imbibition curves for these models are indistinguishable (Figure 14b,c). There is, however, a distinct difference in residual oil saturation between the two scenarios as water wet imbibition results in a residual oil saturation of 25% while fractionally wet imbibition results in a residual oil saturation of 40%, which is more apparent in the capillary pressure curves (Figure 15).

The results and trends for the rounded micrite models (Figures 14d,e,f and 15d,e,f) reflect the results of the rhombic crystal models. Oil relative permeability curves during drainage show slightly different behaviours depending on total porosity, while imbibition curves are indistinguishable. Moreover, the trends and curves for the two different crystal fabrics cannot be distinguished from each other and so rounding the micrite crystals appears to have little to no effect on multi-phase flow properties in comparison to the rhombic counterpart.

Effect of Mesopores within a Micritic Matrix

Model Fabric Properties

The synthetic moldic mesopores modelled in this study were all located in the centre of each octant within the model. Therefore, as the mesopore radii are increased, the distance separating the mesopores decreases (Figure 16, Table 4). The only model in which the mesopores are forced to touch and create a permeable pathway without micropores is in model M45 (Figure 16e) where mesopores have a radius of 45μm. This model is a purely synthetic, conceptual example to examine the change in behaviour upon introduction of a

584 connected mesopore network. In all other models, the mesopores are generated such that
585 they are separate bodies (Figure 16a-d, Table 4) with separation distance decreasing to
586 just a single grid voxel in model M40 (Figure 16d). As such the connectivity between the
587 mesopores in models M10 to M40 (mesopores of less than 40μm radius), is determined by
588 the presence of micropores, as shown in the cross-section through the 30μm radius model
589 (Figure 16f). This style of connectivity is observed in epoxy resin cast images (Figure 1b)
590 and additionally, the moldic mesopore in Figure 1b shows a rough topography around its
591 perimeter which is caused by micrite. This rough topography is captured by the model,
592 again, as shown in Figure 16f.

593 **Pore Network Properties**

594 The mesopores in models M10 to M40 are very well connected by micropores (Figure 16f),
595 without which, they would otherwise be isolated. This variation in connectivity (topology)
596 with mesopore separation (and size) is best examined using the average and maximum
597 coordination numbers (Figure 17).

598 Upon introduction of the mesopores (10μm radius, model M10) to the micritic matrix,
599 average coordination number increases and then progressively decreases with increasing
600 mesopore radius (Figure 17a). The increase in average coordination number is because the
601 10μm radius mesopores connect to a large number of micropores initially. However, as the
602 mesopores increase in size, there are more micropores connected to the mesopore edge
603 (increase in maximum coordination number, Figure 17b) and each micropore that connects
604 to a mesopore has, on average, half of the 3D possible connections by connecting to a
605 single mesopore rather than potentially being connected to multiple additional micropores,
606 as those found in the centre of the micropore matrix do. Hence, the average coordination
607 number decreases. However, the variation in average coordination number for each matrix
608 porosity is only 0.1. The average coordination number is calculated by frequency of

609 occurrence and as such is dominated by the most common pore size, here, micropores.
610 Although pores with larger and larger coordination numbers are present as mesopore radii
611 increases (Figure 17b), the coordination number is still dominated by the matrix porosity
612 whose presence decreases with increased mesopore radius.

613 As would be expected, the maximum coordination number for the models was found to
614 decrease with increasing matrix porosity (Figure 17b) and increase with mesopore radius
615 such that the maximum coordination number exceeded 1300 in the 40μm radii mesopore
616 model with 18% matrix porosity (Figure 17b). The maximum coordination number
617 decreases for 45μm radii mesopores because these pores are overlapping and as such are
618 not entirely surrounded by micropores, reducing the maximum coordination number.

619 **Porosity and Single-phase Permeability**

620 As mesopore radius increases, the relative proportion of the total porosity that is
621 microporosity within the models decreases (Figure 18a, also termed vug-porosity ratio by
622 Lucia 1983, 2007) and as would be expected the overall effect of the presence of
623 mesopores within a microporous matrix is to increase single-phase permeability (Figure
624 18b).

625 As mesopore size increases, the variation in permeability with matrix porosity decreases, as
626 indicated by the black boxes in Figure 18b: the spread of permeabilities is lower for large
627 mesopores than for smaller or no mesopores showing that increasingly larger mesopores
628 influence flow more relative to the matrix flow. The restriction in magnitude of permeability
629 enforced on the fabrics when the micropores provide the only connectivity between the
630 mesopores is further highlighted in Figure 18c. The mesopores can be seen to add porosity
631 to the models but have a limited effect on permeability for models with mesopores up to
632 30μm in diameter.

When mesopore diameter increases to 40μm diameter, there is a distinct increase in both porosity and permeability that deviates from the trends shown in Figure 18c, indicating that the mesopores are influencing flow. Despite being separated in the model (Table 4), upon the introduction of matrix to the models, these mesopores can become directly connected, albeit through a single micropore, explaining this sharp increase in permeability.

Upon forced connection (overlap) of the mesopores at 45μm radius, all models see permeability increase by three orders of magnitude as would be expected for a straight capillary tube, with little variation due to matrix porosity (Figure 18b,c). Due to the larger capillary pressures required for flow in the micropores compared to the mesopores, no such flow takes place, and as such, in these models flow completely bypasses the micropores.

Multi-phase Flow

From Figure 19 and Figure 20 it is clear that the presence of mesopores within the microporous matrix, and indeed the different sizes of mesopores, greatly impact multi-phase flow. Multi-phase flow properties can be seen to vary significantly across the range of models generated.

Since the 45μm radii mesopore model is purely conceptual, its multi-phase flow results are illustrated for drainage only to show the change in behaviour through connected mesopores. For all other models during drainage (Figure 19a,d,g), with increasing mesopore size (direction of arrow) there is a decrease in oil relative permeability at the same saturation. The opposite trend can be seen in the water relative permeability curves. This occurs because the larger mesopores are filled with oil quicker than the smaller mesopores because they are separated by thinner zones of micropores (Table 4). When mesopores are filled, water saturation decreases hugely, however there is still no permeable pathway from inlet to outlet so the relative permeability of oil remains lower in

models with larger mesopores than in models with smaller mesopores. This process is also linked to the trend that as mesopore radius increases, the relative permeability curves become more step-like. This is best observed for the 30μm mesopore model water relative permeability curve (Figure 19g), indicating a more heterogeneous pore system and the successive invasion of mesopores with oil. Sections of the curve with a much steeper gradient indicate slow drainage (a slower decrease in water saturation) as the oil is forced through the microporous horizons between mesopores. Sections of the curves with a much shallower gradient (boxes) indicate a sharp decrease in water saturation and the drainage of oil into a mesopore.

During water wet imbibition, these step wise relative permeability curves are not observed and this is related to trapping. During imbibition the smallest pores fill first which, due to the fabric of the models, results in a connected pathway from inlet to outlet through the micropores, bypassing the mesopores. As such, the oil filled mesopores become trapped, never being drained of their oil and the step wise saturation changes are not observed. This trapping effect results in an increase in residual oil with increasing mesopore size, where the volume of the pore system contained within the mesopores increases (Figure 21a). In other words, with an increase in homogeneity (more pores of a single type, here micropores, fewer mesopores) there is an improved sweep. Residual oil can also be seen to decrease with an increase in matrix porosity (Figure 20b,e,h and Figure 21).

The water-wet imbibition results for models with 40μm radius mesopores, however, disregard this trend and this is probably because the pores are only disconnected from the outlet (and each other) by a single row of voxels. As such, when merged with the microporous matrix, some of the mesopores then become directly connected to the outlet (and each other) and are able to drain of oil, considerably decreasing residual oil saturation. This effect is interesting but it should be noted that such models are not representative

682 elemental volumes as the number of unconnected mesopores may decrease to one, or
683 even zero.

684 Under a fractionally oil wet imbibition scenario, quite the opposite trend can be observed.
685 With increasing mesopore radius, a decrease in residual oil occurs (Figure 20c,f,i and
686 Figure 21b). As previously mentioned, under a fractionally wet scenario oil wettability is
687 randomly distributed amongst 50% of the pores, independently of any of their physical
688 properties (shape, size etc.). As such, statistically half of the mesopores will be oil wet,
689 allowing the development of oil films meaning oil drainage can continue from some
690 mesopores even while water saturation is high. As mesopore size increases, the relative
691 proportion of oil that can be drained through oil wet mesopores increases and so residual
692 oil is lower for models with larger mesopores (Figure 20f,i). Of course, this is a statistical
693 distribution of wettability and as such some models do not conform to this trend (e.g. Figure
694 20c, 30μm radii model).

695 **DISCUSSION**

696 Through investigation of the effect of micropore size and total matrix porosity it has been
697 shown that the new object based rock reconstruction algorithm used to model micritic
698 microporous carbonate fabrics is able to capture the basic textural properties that control
699 macro-scale single-phase permeability in these rock fabrics. There is a very good match
700 between modelled single-phase permeability and measured porosity-permeability data
701 (Figure 13a) reported for the microporous facies of the Middle Eastern Lower Cretaceous
702 Shuaiba formation (Fullmer et al., 2014). The pore size distributions captured in the models
703 (Figures 7a-c, 12a-c) are uni-modal which is not necessarily characteristic of the full
704 variation of pore sizes present in microporous carbonates. As these models focus on
705 micrite dominated fabrics only, this uni-modal and narrow distribution of pore size is not
706 unexpected as the models represent essentially homogeneous fabrics. However, the most

volumetrically significant pore diameter in the purely micritic models generated here (0.70-0.80μm diameter) is equivalent to the pore size of the Type 1 micropores described in both the Arab D (Clerke et al., 2008) and Shuaiba Formation (Fullmer et al., 2014), where this pore type is both the largest micropore size and again the most volumetrically significant in these samples. Smaller micropores that are reported in the literature are below the resolution of the model and as such cannot be captured here, but are thought to make an insignificant contribution to flow (Clerke et al., 2008). Similarly, the capillary pressure curves in Figures 9d-f, 15 and 20 show ranges that are not out with the range expected within reservoirs as has previously been shown in measured relative permeability data (e.g. Øren et al., 2001; Okasha and Funk, 2002; Al Waili, 2009).

We have aimed to represent some of the different micritic fabrics of microporous carbonates by varying micropore size, total matrix porosity, crystal rounding and the presence of mesopores within the microporous matrix. All such variations can be observed in natural samples. Since modelling micropores requires sub-micron resolution, being able to either observe or represent micropores within a multi-scale network is a formidable challenge. Indeed, in all digital rock reconstructions there is a trade-off between the spatial resolution of the model and the largest (or smallest) scale of feature that can be examined. The upper limits of computational power and memory restrict firstly the number of voxels in a model and therefore the physical volume of a model that can be created, and secondly restrict the grid volume through which fluid flow can be simulated. As such, while a higher model spatial resolution allows features to be more finely resolved, a higher resolution significantly reduces the physical model size that can be held within the memory limits of the machine being used since the 3D model size increases as the cube of the number of voxels along each axis.

731 The developed algorithm is used to generate end-point micritic fabrics; rhombic and
732 rounded micrite. In order to do so, the form of the micrite crystals is simplified to a euhedral,
733 cubic form. However, the morphology of the modelled euhedral crystal fabrics (in thin
734 section and in pseudo-3D) can be seen to be reasonable when compared to real rocks
735 (Figure 5). The biggest shortcoming of the model is the discretisation which results in
736 rugose crystal edges, reducing the euhedral or spherical nature of the crystals, and the
737 lower the resolution (or smaller the crystal size) the more extreme the effect (Figure 5c,d).
738 However, the model is still capable of replicating measured permeability data (Figure 13a)
739 thus highlighting its ability to capture the major fabric controls on single-phase flow in these
740 fabrics. With ever increasing computational power, the inherent flexibility of the method
741 would allow higher resolution models and larger scale features of microporous carbonates
742 (such as macropores, fractures and fissures) to be incorporated with ease and further
743 studies on the petrophysical properties of such fabrics could be performed.

744 While examining the effect of micropore size on flow it has been observed that even at
745 these model scales, single-phase permeability shows a dependence on (average) pore size
746 (Figure 8). An increase in average pore radius from 0.26μm to 0.44μm yields an increase in
747 permeability from 1.7md to 2.7md respectively. Despite the positive trend between average
748 pore size and permeability, this range in permeability across all models is small (~1md).

749 Models generated at the lowest resolution of 0.50μm^3/voxel (model r_5) had the largest
750 average pore size (0.44μm diameter) and exhibited a change in pore network properties in
751 comparison to the models at higher resolutions, showing a larger percolation radius (Figure
752 7b). While the distinct increase in percolation threshold and connectivity between models r_4
753 and r_5 (Figure 7) does not translate to a similar increase in single-phase permeability
754 between the two models, it is a possible reason for the lower residual oil saturation of model
755 r_5 (Figure 9e,f). The increased percolation threshold and pore size may contribute to

reduced trapping. Multiphase flow properties across models r_1 to r_5 showed a small decrease in residual oil with increasing average pore size and similarly, oil relative permeability curves exhibited small variations across all models while water relative permeability curves were indistinguishable (Figure 9). These results suggest that average pore size is affecting multi-phase flow in these models.

Models r_1 to r_4, have been shown to have very similar percolation thresholds. This similarity in pore network structure suggests that model r_4 has approximately the same physical pore scale flow as the pore network in model r_1, where the average pore radius of 0.26μm (Table 2) is closer to the minimum diameter of the micropores that are observed in the epoxy resin cast (Figure 1b). Indeed, the match between the modelled and measured single-phase permeability data reported for models r_a through r_e further corroborates that modelling the microporous fabrics at a resolution of 0.40μm^3/voxel (that of model r_4) captures the relevant pore scale features that exist within real microporous carbonate fabrics and that control single-phase permeability. These results provide a method that allows larger physical volumes to be modelled, and to incorporate micropores into a more multi-scale network, by modelling at a resolution of 0.40μm^3/voxel. At this resolution it was shown that total matrix porosity and therefore pore size, affects single-phase permeability by an order of magnitude (0.6md to 7.5md) over the range of porosities examined (18-35% respectively, Figure 13). Increasing matrix porosity, however, has very little effect on multi-phase relative permeability and residual oil saturation under both the strongly water wet and fractionally wet wettability scenarios (Figure 14). The effect of micrite rounding has also been examined here. At approximately the same porosity (30%, indicated by the arrows in Figure 13b), the permeability in a rounded micrite model can be seen to be approximately 1md higher than in a rhombic crystal model, most probably due to the increase in pore size after rounding. Comparing a rhombic matrix to its rounded counterpart (dashed lines, Figure 13b) shows

781 an increase in porosity of 7-8%, in agreement with the increase in porosity due to rounding
782 reported by Lambert et al (2006). A corresponding substantial increase in single-phase
783 permeability, up to an order of magnitude for the lowest porosity models is also observed
784 (Figure 13). As such, if a reservoir was of constant micropore volume within the rhombic
785 fabrics, rounding of the original fabric would result in an alteration of the single-phase
786 permeability due to the increase in pore size, as indicated by these results and in
787 agreement with Lambert et al (2006). Conversely micrite rounding can be seen to have a
788 limited effect on multi-phase flow under these wettability scenarios (Figure 14) suggesting
789 that micrite rounding has little to no effect on the pore network topology in comparison to
790 the pore networks within rhombic micrite.

791 These results suggest that while end-point micritic morphologies have implications for
792 single-phase permeability, resulting pore size changes do not affect multi-phase flow
793 properties. Despite an extensive nomenclature being established to describe varying
794 microporous carbonate fabrics (for example Deville de Periere et al., 2011, Fullmer et al.,
795 2014), the definition of only two fabrics 'classes' maybe necessary to discriminate distinct
796 petrophysical behaviours or rock types. Of course, the degree of wettability alteration (if
797 any) may vary in these fabrics as rounded micrite fabrics are expected to have a higher oil
798 saturation as they are found higher in the oil column (Lambert et al., 2006). Further analysis
799 is still required here.

800 At a resolution of 0.40μm^3/voxel it is possible to include up to three orders of magnitude of
801 pore size variation through the inclusion of meso-scale pores (>10μm diameter). Results
802 have shown that the addition of mesopores to a micritic matrix greatly impacts the geometry
803 and topology of the pore system (Figure 17). Single-phase permeability increases with
804 mesopore radius (Figure 18). The relationship between single-phase permeability and
805 mesopore radius is non-linear but is related to the separation distance between the

806 mesopores. Micropores dominate single-phase permeability magnitude where the only
807 permeable connection between mesopores is through the microporous matrix (models M10
808 to M30). Single-phase permeability is limited to less than 20md for these models. A distinct
809 increase in single-phase permeability for models with mesopores of 40μm radii is due to the
810 single voxel separation between the mesopores. At such small separation distances the
811 mesopores may be connected by a single or a few micropores (Table 4) and therefore may
812 be considered directly connected, as is suggested by the capillary pressure data (Figure
813 19). For models with mesopores of 45μm radius the effect of direct mesopore connectivity
814 is even more pronounced and permeability increases by three orders of magnitude as flow
815 is able to completely bypass the microporous matrix. Similar observations were made by
816 Anselmetti et al (1998). We are aware that in reality not all mesopores in a reservoir have
817 the same shape and size. Here, the mesopore models are entirely synthetic and the
818 porosities of the models with the largest mesopores are beyond the porosities typically
819 observed in these types of carbonates (Figure 18a). However, such models are useful for
820 examining the end-member properties of these fabrics.

821 The multi-phase flow properties of the moldic mesopore models also vary significantly with
822 both mesopore size and matrix porosity and it has been shown that these results are again
823 related to the separation distance between mesopores and the relative proportion of
824 microporosity in the models. Most importantly, under a water-wet imbibition scenario, an
825 increase in homogeneity (more micropores, fewer mesopores) increases the sweep
826 (microscopic displacement efficiency) of the model (Figure 21a). This previously has been
827 reported by other authors in fabrics where micropores are present (Clerke et al., 2009;
828 Fung et al., 2011; Hollis et al., 2010; Fullmer et al., 2014) and is also observed in the water
829 wet imbibition capillary pressure curves in Figure 20b,e,h.

830 Finally, across all different fabrics it has been shown that wettability scenario during

imbibition impacts residual oil. The wetting state of any rock is extremely hard to determine as core wettability experiments are expensive (both in time and money), and more importantly it is difficult to ensure that the core wettability under lab conditions is the same as in-situ subsurface conditions. Relative permeability data are therefore difficult to acquire under reservoir conditions. If such data are available, they are usually only for one particular bulk plug sample while the wetting state of a carbonate may vary at much smaller (pore scale) and indeed larger scales. Modelling two phase flow under a variety of different wettability scenarios is one possible way to understand how the fluid flow properties would vary under different wetting states. Wettability dependent variation in multi-phase flow properties and residual oil has been demonstrated in this study by looking at strongly water wet imbibition and fractionally oil wet imbibition. The multi-phase flow results for models with varying sizes of mesopores clearly demonstrates the dependency of recovery on wetting scenario (Figure 21).

However, the wetting state of a real rock may not be randomly distributed throughout the pore network as is simulated for the fractionally wet wettability case here. Intermediate wettability (where part of the pore system is water-wet and the remainder oil-wet) maybe controlled by the pore size or pore shape (degree of curvature), or by mineralogy (Kovscek et al., 1993; Skauge et al., 2004). The mineralogy of the micrite in these microporous carbonate models does not vary, and as such mineralogy does not need to be considered as a controlling factor on wettability alteration. Pore size and shape, however, are viable controls on wettability. While network models are able to determine wetting alteration due to pore size, they are rarely able to model wettability alteration due to changes in pore shape and curvature as defined by the extracted pore network. Blunt (1998) introduced a network model capable of modelling wettability based on pore shape parametrically, but a network model capable of modelling fluid layers that are dependent on pore shape as defined in the

pore network, is vital if we are to be able to predict multi-phase flow properties of carbonates and indeed, other media. Such a network model has been developed by Kallel et al (2014) and preliminary results suggest that incorporating pore shape through degree of curvature into a multi-phase flow simulation generates different results to otherwise. Under a wetting state controlled by pore shape, the multi-phase properties of rounded micrite compared to rhombic micrite may indeed be very different. An additional aspect which requires further investigation is the variation in multi-phase flow properties under different initial water saturations. Here, minimum initial water saturations of 0.07 have been used during simulation. This may be low as initial water saturations are reported to be around 5-15% for micritic microporous carbonate fabrics (Sallier and Hamon, 2005; Masalmeh and Jing, 2007).

This study has demonstrated the flexibility of the developed algorithm to explore the variations in the petrophysical properties of microporous fabrics and it provides a basis to further develop future studies. By methodologically altering end-point parameters of the rock fabrics and additionally adjusting the fluid and wetting properties of the models, it will be possible to build a state-space of how the petrophysical properties of microporous carbonates vary under these different fabrics and use the trends to predict single-phase and multi-phase flow. The addition of high quality 3D images through FIBSEM or nano-CT could be used to further validate the multi-phase properties observed here.

SUMMARY AND CONCLUSIONS

A flexible, object-based rock reconstruction algorithm has been developed that reproduces the micro-scale micritic fabrics of microporous carbonates. The algorithm was utilised to explore the effects of micropore size, total microporosity, micritic rounding and the presence of moldic mesopores on both single- and multi-phase fluid flow properties within a micritic matrix. For all models, multi-phase flow was simulated under both a 50% fractionally oil–wet

881 and strong water-wet imbibition scenario.

882 Micropore size was controlled by varying model resolution from 0.10-0.50μm^3/voxel and all
883 models had approximately 26% porosity. Average pore radius varied between 0.26μm up to
884 0.44μm across the resolutions, and was found to have a positive correlation with single-
885 phase permeability which varied between 1.7md and 2.7md respectively. All models
886 displayed similar multi-phase flow properties and an overall trend of decreasing residual oil
887 with increasing average pore radius was observed.

888 Total microporosity has been shown to influence single-phase permeability significantly
889 over the range of porosities modelled (18-35%). An order of magnitude increase in
890 permeability can be attributed to the resulting increase in pore size. These results indicate
891 that microporosity can conduct significant single-phase permeabilities of up to 7.5md, in
892 agreement with measured data reported in the literature. Total microporosity was, however,
893 shown to have little to no effect on imbibition behaviour and oil recovery in these models.
894 Similarly the effect on multi-phase flow properties of rounding micrite crystals within the
895 matrix was limited, especially during imbibition.

896 As expected, rounded micritic fabrics show an increase of up to 8% in porosity and up to an
897 order of magnitude increase in single-phase permeability in comparison to precursor
898 rhombic micritic fabrics. However, more importantly the overall porosity-permeability trends
899 exhibit an increase in single-phase permeability at a given porosity again indicating the
900 control on single-phase flow properties exerted by micropore size. Multi-phase flow
901 properties however remain unaltered between the rhombic crystal fabric and the rounded
902 model fabric.

903 Finally it has been shown that within micritic matrix, moldic mesopores only affect single-
904 phase permeability if they are directly connected to each other. If the mesopores are

separated by microporous matrix, permeability is controlled by the micropores. Such fabrics have been shown to conduct permeabilities of up to 20md, demonstrating that the contribution of microporosity to single-phase permeability cannot be overlooked within multi-scale carbonate pore systems. During multi-phase flow under a strongly water-wet imbibition scenario, it has been shown that fabrics with a high fraction of microporosity to total porosity retain a much lower residual oil saturation during water wet imbibition. Under this wettability scenario, the presence of microporosity within a carbonate reservoir is desirable, as it increases the sweep of the reservoir during imbibition.

Micropores are found within many different carbonate rock fabrics and often in combination with other scales of porosity. While this study has examined only a small part of the full spectrum of known fabric variations and indeed different hypothetical wettability scenarios, it has demonstrated the breadth of single-phase and multi-phase flow properties that can occur in these fabrics. These results confirm that it is important to consider the role of micropores in fluid flow when assessing the producibility of microporous carbonates. The algorithm developed here offers a flexible platform with which to probe the full spectrum of microporous carbonate fabrics that occur in hydrocarbon reservoirs and to concurrently examine the variable geologically controlled wettability scenarios.

REFERENCES

Al-Kharusi, A. S., and M. J. Blunt, 2008, Multi-phase flow predictions from carbonate pore space images using extracted network models, Water Resources Research, V.44

Al Waili, I. H., 2009, Developing Generalised Capillary Pressure Curves and Saturation Height Function for Shuaiba Carbonate Reservoirs in Field A, Society of Petroleum Engineers, doi:10.2118/136191-STU

Al-Yousef, H. Y., P. M. Lichaa, A. U. Al-Kaabi, and H. Alpustun, 1995, Wettability

929 Evaluation of a Carbonate Reservoir Rock from Core to Pore Level, SPE Conference,
930 Bahrain, SPE19885

931 Anselmetti, F. S, S. Luthi, and G. P. Eberli, 1998, Quantitative Characterisation of
932 Carbonate Pore Systems by Digital Image Analysis, AAPG Bulletin, V. 82, p1815-1836

933 Bakke, S., and P-E. Øren, 1997, 3-D Pore-Scale Modelling of Sandstones and Flow
934 Simulations in the Pore Networks, SPE Journal, v. 2.

935 Barenblatt, G. I., T. W. Patzek, and D. B. Silin, 2003, The mathematical model of
936 nonequilibrium effects in water-oil displacement, SPE Journal, volume 8 (4), p409--416

937 Biswal, B., P-E. Øren, R. Held, S. Bakke, and R. Hilfer, 2007, Stochastic multi-scale model
938 for carbonate rocks, Physical Review E 75, 061303.

939 Biswal, B., R. J. Held, V. Khanna, J. Wang, and R. Hilfer, 2009a, Towards precise
940 prediction of transport properties from synthetic computer tomography of reconstructed
941 porous media, Physical Review E 80, 041301.

942 Biswal, B., P-E. Øren, R. Held, S. Bakke, and R. Hilfer, 2009b, Modelling of multi-scale
943 porous media, Image Analysis and Stereology 28, p23-34.

944 Blunt, M., 1998, Physically-based network modelling of multi-phase flow in intermediate-wet
945 porous media, Journal of Petroleum Science and Engineering, 20, p117-125

946 Blunt, M. J., B. Bijeljic, H. Dong, O. Gharbi, S. Iglauer, P. Mostaghimi, A. Paluszny, and C.
947 Pentland, 2013, Pore-scale imaging and modelling, Advances in Water Resources, Volume
948 51, P. 197-216, ISSN 0309-1708

949 Bobek, J. E., C. C. Mattax, and M. O. Denekas, 1958, Reservoir Rock Wettability - Its
950 Significance and Evaluation, Society of Petroleum Engineers.

951 Buchgraber, M., M. Al-Dossary, C. M. Ross, and A. R. Kovscek, 2012, Creation of a dual-

952 porosity micromodel for pore-level visualization of multi-phase flow, Journal of Petroleum
953 Science and Engineering, 86, 27-38.

954 Budd, D., 1989, Micro-rhombic calcite and microporosity in limestones: a geochemical
955 study of the lower cretaceous Thamama group, UAE, Sedimentary Geology, v. 633-4,
956 p293-311.

957 Cantrell, D. L. and R. M. Hagerty, 1999, Microporosity in Arab formation carbonates, Saudi
958 Arabia, GeoArabia 4, p129 - 154.

959 Chilingar, G.V. and T. F. Yen, 1983, Some Notes on Wettability and Relative Permeabilities
960 of Carbonate Reservoir Rocks, II, Energy Sources, Vol. 7.

961 Choquette, P., and L. Pray, 1970, Geologic Nomenclature and Classification of Porosity in
962 Sedimentary Carbonates, AAPG Bulletin, v. 542, p207-250

963 Chun, B. and A. J. C. Ladd, 2007, Interpolated boundary condition for lattice Boltzmann
964 simulations of flows in narrow gaps, Phys. Rev. E 75

965 Clerke, E. A., H. W. Mueller III, E. C. Phillips, R. Y. Eyvazzadeh, D. H. Jones, R.
966 Ramamoorthy, and A. Srivastava, 2008, Application of Thomeer Hyperbolas to decode the
967 pore systems, facies and reservoir properties of the Upper Jurassic Arab D Limestone,
968 Ghawar field, Saudi Arabia: A “Rosetta Stone” approach, GeoArabia, 13(4), 113-160

969 Clerke, E. A., 2009, Permeability, relative permeability, microscopic displacement
970 efficiency, and pore geometry of M_1 bimodal pore systems in Arab D Limestone, SPE
971 Journal, 14(3), 524-531

972 Clerke, E. A., J. J. Funk, and E. Shtepani., 2013, Spontaneous Imbibition of Water into Oil
973 Saturated M_1 Bimodal Limestone, IPTC 2013: International Petroleum Technology
974 Conference

975 Clerke, E. A., D. F. Allen, S. C. Crary, A. Srivastava, R. Ramamoorthy, P. Saldungaray, P.
976 Savundararaj, D. Helliot, J. Goswami, and G. Bordakov, 2014, Wireline Spectral Porosity
977 Analysis of the Arab Limestone—From Rosetta Stone to Cipher. Society of Petrophysicists
978 and Well-Log Analysts.

979 Cnudde, V., and M. N. Boone, 2013, High-resolution X-ray computed tomography in
980 geosciences: A review of the current technology and applications, Earth-Science Reviews,
981 Volume 123, Pages 1-17, ISSN 0012-8252

982 Cox, P., R. Wood, J. A. D. Dickson, H. B. Al-Rougha, H. Shebl, and P. W. M. Corbett, 2010,
983 Dynamics of cementation in response to oil charge: Evidence from a Cretaceous carbonate
984 field, U.A.E., Sedimentary Geology, v228(3-4), p246-254

985 Cuiec, L., 1984, Rock/crude-oil interactions and wettability: An attempt to understand their
986 interrelation, Society of Petroleum Engineers, Vol. 13211

987 Darcy, H., 1856, Les Fontaines Publiques de la Ville de Dijon, Dalmont, Paris

988 Desplat, J. C., I. Pagonabarraga, and P. Bladon, 2001, LUDWIG: A parallel Lattice-
989 Boltzmann code for complex fluids, Computer Physics Communications, v. 1343. p273-290

990 Deville de Periere, M., C. Durlet, E. Vennin, L. Lambert, R. Bourillot, B. Caline, and E. Poli,
991 2011, Morphometry of micrite particles in cretaceous microporous limestones of the Middle
992 East: Influence on reservoir properties, Marine and Petroleum Geology, 289, p1727-1750.

993 Dodd, N., R. Marathe, J. Middleton, A. Fogden, A. Carnerup, M. Knackstedt, K. Mogensen,
994 X. Marquez, S. Frank, N. Bounoua, and R. Noman,2014, Pore-Scale Imaging of Oil and
995 Wettability in Native-State, Mixed-Wet Reservoir Carbonates. Paper presented at the
996 International Petroleum Technology Conference, Doha, Qatar

997 Dravis, J. J., 1989, Deep-burial microporosity in upper Jurassic Haynesville oolitic
998 grainstones, East Texas, Sedimentary Geology, Volume 63, Issues 3–4, Pages 325-341.

999 Ehrenberg, S., O. Walderhaug, and K. Bjørlykke, (2012). AAPG Bulletin, v. 96, no. 2, p.
1000 217–233

1001 Folk, R. L., 1962, Classification of carbonate rocks, AAPG memoirs, 1, p62-84.

1002 Fullmer, S. M., S. A. Guidry, J. Gournay, E. Bowlin, G. Ottinger, A. M. Al-Neyadi, and E.
1003 Edwards, 2014, Microporosity: Characterization, Distribution, and Influence on Oil
1004 Recovery, International Petroleum Technology Conference Abstract.

1005 Fung. L., U. Middya, and A. Dogru, 2011, Numerical Simulation of Fractured Carbonate
1006 Reservoirs with the M_1 Bimodal Pore System, Society of Petroleum Engineers, SPE
1007 142296

1008 Funk, J. J., and A. M. Al-Harbi, 2009, Modeling Complex Dispersive Capacitance in
1009 Carbonates using NMR T2 Distributions, SPE Saudi Arabia Section Technical Symposium,
1010 Society of Petroleum Engineers

1011 Heasley, E. C., R. H. Worden, and J. P. Hendry, 2000, Cement distribution in a carbonate
1012 reservoir: recognition of a palaeo oil–water contact and its relationship to reservoir quality in
1013 the Humbly Grove field, onshore, UK, Marine and Petroleum Geology, Volume 17, Issue 5,
1014 p639-654

1015 Hollis, C., V. Vahrenkamp, S. Tull, A. Mookerjee, C. Taberner, and Y. Huang, 2010, Pore
1016 system characterization in heterogeneous carbonates: An alternative approach to widely-
1017 used rock-typing methodologies, Petroleum Geoscience 27, p772-793.

1018 Hurley, N., T. Zhang, W. Zhao, and G. Xu, 2011, Method to build 3D digital models of
1019 porous media using transmitted last scanning confocal microscopy and multi-point
1020 statistics, US Patent: US 2011/0004447 A1

1021 Jiang, Z., K. Wu, G. D. Couples, M. I. J. van Dijke, and K. S. Sorbie, 2007, Efficient
1022 extraction of networks from 3D porous media, Water Resource Research, 43, W12S03.

1023 Kallel, W., R. van Dijke, K. Sorbie, R. Wood, Z. Jiang, and S. Harland, 2014, Modelling
1024 Wettability Alteration in Microporous Carbonate Rocks, AAPG Abstract, #41428

1025 Kashfi, M., 1974, A Brief Study of Reservoir Rock Wettability in the Iranian Oil Fields,
1026 Energy Sources, Vol. 1

1027 Kirkham, A., M. Bin Juma, T. A. M. McKean, A. F. Palmer, M. J. Smith, A. H. Thomas, and
1028 B. N. Twombley, 1996, Fluid saturation prediction in the 'transition zone' carbonate
1029 reservoir, Abu Dhabi, Geoarabia 1, p551-566

1030 Knackstedt, M. A., W. V. Pinczewski, A. Fogden, and T. Senden, 2011, Improved
1031 characterization of EOR processes in 3D. Characterizing mineralogy, wettability and
1032 residual fluid phases at the pore scale, Society of Petroleum Engineers,
1033 doi:10.2118/145093-MS

1034 Kovscek, A. R., H. Wong, and C. J. Radke, 1993, A pore-level scenario for the development
1035 of mixed wettability in oil reservoirs, AIChE Journal, 39(6), p1072-1085

1036 Lambert, L., C. Durlet, J-P. Loreau, and G. Marnier, 2006, Burial dissolution of micrite in
1037 Middle East carbonate reservoirs Jurassic-Cretaceous: keys for recognition and timing,
1038 Marine and Petroleum Geology 231, p79-92.

1039 Lichaa, P. M., H. Alpustun, J. H. Abdul, W. A. Nofal and A. B. Fuseni, 1993, Wettability
1040 evaluation of a carbonate reservoir rock, Advances in Core Evaluation III, Reservoir
1041 Management, Vol.327

1042 Lucia, F. J., 1983, Petrophysical Parameters Estimated From Visual Descriptions of
1043 Carbonate Rocks: A Field Classification of Carbonate Pore Space, Society of Petroleum
1044 Engineers, doi:10.2118/10073-PA

1045 Lucia, F. J., 2007, Carbonate reservoir characterisation: an integrated approach (2nd.
1046 Edition), Springer

1047 Lucia, F. J. and R. G. Loucks, 2013, Micropores in carbonate mud: early development and
1048 petrophysics, GCAGS Journal, Volume 2, p1-10

1049 Marathe, R., M. L. Turner, and A. Fogden, 2012, Pore-Scale Distribution of Crude Oil
1050 Wettability in Carbonate Rocks. Energy & Fuels, 26(10), p.6268-6281

1051 Masalmeh, S. K., and X. Jing, 2007, Improved Characterisation And Modelling Of
1052 Carbonate Reservoirs For Predicting Waterflood Performance. International Petroleum
1053 Technology Conference. doi:10.2523/11722-MS

1054 Morrow, N. R., 1976, Capillary Pressure Correlations for Uniformly Wetted Porous Media,
1055 Petroleum Society of Canada

1056 Moshier, S., 1989a, Development of microporosity in a micritic limestone reservoir, lower
1057 cretaceous, Middle East, Sedimentary Geology 633-4, p217-240

1058 Moshier, S. O., 1989b, Microporosity in micritic limestones: a review, Sedimentary Geology
1059 63, p191-213.

1060 Okabe, H., and M. Blunt, 2004, Prediction of permeability for porous media reconstructed
1061 using multiple-point statistics, Physical Review E, 70, 066135

1062 Okasha, T.M., J. Funk, and Y. S. Baloboid, 2001, Wettability and relative permeability of
1063 Lower Cretaceous carbonate rock reservoir, Saudi Arabia, Society of Core Analysts, SCA
1064 2001-03

1065 Okasha, T.M., and J. Funk, 2002, Electrical and petrophysical properties of Shu'aiba
1066 reservoir, Saudi Arabia, Society of Core Analysts, SCA 2002-48

1067 Okasha, T.M., J. J. Funk and H. N. Rashidi, 2007, Fifty Years of Wettability Measurements
1068 in the Arab-D Carbonate Reservoir. Paper presented at the SPE Middle East Oil and Gas
1069 Show and Conference, Kingdom of Bahrain

1070 Øren, P-E., S. Bakke, and O. Arntzen, 1998, Extending predicative capabilities to network
1071 models, SPE Journal 3, 324-336

1072 Øren, P-E. and S. Bakke, 2003, Reconstruction of Berea sandstone and pore-scale
1073 modelling of wettability effects, Journal of Petroleum Science and Engineering 39, p177–
1074 199

1075 Pittman, E. D., 1971, Microporosity in Carbonate Rocks: geological notes, AAPG Bulletin,
1076 5510, p1873-1878.

1077 Richards, J., J. P. Sizun, and L. Machhour, 2007, Development and compartmentalisation
1078 of chalky carbonate reservoirs: The Urgonian Jura-Bas Dauphine platform model (Genissiat
1079 southeastern France), Sedimentary Geology, 198, p195-207

1080 Roth, S., B. Biswal, G. Afshar, R. Held, P-E. Øren, L. Berge, and R. Hilfer, 2011,
1081 Continuum-based rock model of a reservoir dolostone with four orders of magnitude in pore
1082 sizes, AAPG Bulletin, 956, p925-940.

1083 Sallier, B., and G. Hamon, 2005, Micritic limestone of the middle-east: influence of
1084 wettability, pore network and experimental technique on drainage capillary pressure curve,
1085 SCA International Symposium, Toronto, Canada, August, p.21--25

1086 Schneider, C. A., W. S. Rasband, and K. W. Eliceiri, 2012, NIH Image to ImageJ: 25 years
1087 of image analysis, Nature Methods 9, p671-675.

1088 Sengupta, A., P. Hammond, P. Frenkel, and E. Boek, 2012, Error analysis and correction
1089 for Lattice Boltzmann simulated flow conductance in capillaries of different shapes and
1090 alignments, Journal of Computational Physics, 231, p2634–2640.

1091 Smith, L. B., G. P. Eberli, J. L. Masaferro, and S. Al-Dhahab, 2003, Discrimination of
1092 effective from ineffective porosity in heterogeneous Cretaceous carbonates, Al Ghubar
1093 field, Oman, AAPG bulletin, 879, p1509-1529.

1094 Skauge, A., K. Spildo, L. HØiland, B. Vik, and B. Ottesen, 2004, Experimental evidence of
1095 different intermediate wetting states, Society of Core Analysts Paper, SCA2004-04

1096 Skauge, A., A. Sorvik, B. Vik, and K. Spildo, 2006, Effect of wettability on oil recovery from
1097 carbonate material representing different pore classes, Society of Core Analysts Paper,
1098 SCA2006-01

1099 Skauge, A., K. Spildo, L. Høiland, and B. Vik, 2007, Theoretical and experimental evidence
1100 of different wettability classes. Journal of Petroleum Science and Engineering 57(3-4), 321-
1101 333

1102 Torquato, S., 1984, Bulk properties of two-phase disordered media, I. Cluster expansion for
1103 the effective dielectric constant of dispersions of penetrable spheres, J Chem Phys 81.
1104 5079-5088.

1105 Torquato, S., 1985, Bulk properties of two-phase disordered media. II. Effective conductivity
1106 of a dilute dispersion of penetrable spheres. J Chem Phys 83, 4776-4785.

1107 Torquato, S., 1986, Bulk properties of two-phase disordered media, ill. New bounds 98 on
1108 the effective conductivity of dispersions of penetrable spheres, J Chem Phys 84.6345-6359.

1109 Treiber, L. E., and W. W. Owens, 1972, A Laboratory Evaluation of the Wettability of Fifty
1110 Oil-Producing Reservoirs, Society of Petroleum Engineers

1111 Valvatne, P. H., and M. J. Blunt, 2004, Predictive pore-scale modelling of two-phase flow in
1112 mixed wet media, Water Resources Research, 407.

1113 Van Geet, M., R. Swennen, and M. Wevers, 2000, Quantitative analysis of reservoir rocks
1114 by microfocus X-ray computerised tomography, Sedimentary Geology, Volume 132, Issues
1115 1–2, Pages 25-36

1116 Vogel, H.-J., and K. Roth, 2001, Quantitative morphology and network representation of soil

1117 pore structure, Advances in Water Resources, Volume 24, Issues 3–4, Pages 233-242.

1118 Volery, C., D. Davaud, A. Foubert, and B. Caline, 2009, Shallow-marine microporous
1119 carbonate reservoir rocks in the Middle East: Relationship with seawater Mg/Ca Ratio and
1120 eustatic sea level, Journal of Petroleum Geology, Vol.32(4), p313-326

1121 Volery, C., E. Davaud, C. Durlet, B. Clavel, J. Charollais, and B. Caline, 2010, Microporous
1122 and tight limestones in the Urgonian Formation (late Hauterivian to early Aptian) of the
1123 French Jura Mountains: Focus on the factors controlling the formation of microporous
1124 facies, Sedimentary Geology, Volume 230

1125 Wagner, O., 1990, Geochemical stratigraphy and porosity controls in Cretaceous
1126 carbonates ear the Oman mountains, Geological Society, London, Special Publications,
1127 49(1), p127-137

1128 Wu, K., N. Nunan, J. Crawford, I. Young, and K. Ritz, 2004, An efficient Markov chain
1129 model for the simulation of heterogeneous soil structure, Soil Science Society of America
1130 Journal, 68(2), p346

1131 Wu, K., M. I. J. van Dijke, G. Couples, Z. Jiang, J. Ma, K. Sorbie, J. Crawford, I. Young, and
1132 X. Zhang, 2006, 3D stochastic modelling of heterogeneous porous media applications to
1133 reservoir rocks, Transport in Porous Media, v65, p443-476

1134 Wu, K., A. Ryazanov, M. I. J. van Dijke, Z. Jiang, J. Ma, G. Couples, and K. Sorbie, 2008,
1135 Validation of methods for multi-scale pore space reconstruction and their use in prediction
1136 of flow properties in carbonate, Society of Core Analysts Paper, SCA 2008-34

1137

1138

1139

1140

Sophie Harland

Sophie Harland received her B.Sc and M.Sci. Degrees in Geophysics from the School of Earth and Environment, University of Leeds, UK, in 2011. Currently, she is a Ph.D. student at the School of Geosciences, University of Edinburgh, UK.

Rachel Wood

Rachel Wood received a PhD from the Open University in 1987. She has worked on the evolution of reef ecosystems, carbonate diagenesis, and the modelling of carbonate systems at various scales. From 2001-2006 she was a Principal Research Scientist at Schlumberger Cambridge Research, and joined the University of Edinburgh in 2006. Since 2012 she has been Professor of Carbonate Geoscience.

Andrew Curtis

Andrew Curtis received a PhD from the University of Oxford in 1994. He has worked on mathematical and geophysical problems in seismology, imaging and inversion, and in geological expert elicitation. From 1997-2005 he was Senior then Principal Research Scientist at Schlumberger Cambridge Research, and joined the University of Edinburgh in 2005. Since 2009 he has been Professor of Mathematical Geoscience.

Marinus van Dijke

M.I.J. (Rink) van Dijke obtained his PhD (soil science) from Wageningen Agricultural University (The Netherlands) in 1997. He is currently an associate professor in the Institute of Petroleum Engineering at Heriot-Watt University. His main research interest is in pore-scale modelling of multi-phase flow.

Kevin Stratford

Kevin Stratford received his PhD in condensed matter physics from the University of

Leicester in 1993. He is currently seconded to IVEC, Australia from the EPCC at the University of Edinburgh. His research interests include (classical) molecular modelling and coarse-grained methods (especially complex fluids). He also has experience in geophysical fluid dynamics, engineering, and problems with global optimisation.

Zeyun Jiang

Zeyun Jiang received his Ph.D. in petroleum engineering from Heriot-Watt University, UK in 2008. Subsequently he joined the university with a focus on network extraction and characterisation of porous media.

Wissem Kallel

Wissem Kallel holds a Master's degree in Engineering from the Ecole Polytechnique de Tunisie. He is currently a PhD student at the Institute of Petroleum Engineering, Heriot-Watt University, Edinburgh. His research mainly focuses on the pore-scale modelling of wettability in porous media.

Ken Sorbie

Ken Sorbie received his PhD from the University of Sussex in 1972. He has over 30 years of experience in a wide range of oil related research areas and has been based at Heriot-Watt University in the Institute of Petroleum Energy since 1988 where he is Cairn Energy Professor of Petroleum Engineering.

Figure 1 Secondary electron SEM images of microporous carbonate samples from the Early Cretaceous Thamama Group, UAE. (a) Image of a broken chip showing the rhomboidal nature of micrite crystals. (b) Epoxy resin cast showing the sponge like network of micropores and its connectivity with a larger mesopore. The inset shows a high resolution image of the plate-like morphology of the micropores between the facets of three micrite crystals. (c) Image of a broken chip showing rounded micrite crystals and highlighting crystals that exhibit no vertices or facets.

Figure 2 Example back-scatter SEM images of carbonate micropores that can be used to extract quantitative data for model calibration. (a) & (b) Typical backscatter SEM images used for crystal diameter measurements. Both matrix crystals and larger pore filling cement crystals can be seen in this figure. Only the matrix crystal data were used in this study. (c) Crystal size distribution as measured from backscatter images and used to populate models at a resolution of 0.40μm^3/voxel.

Figure 3 (a) 100x100voxel slice through a 25% porosity model demonstrating the crystal overlap created by crystal layering. Edge voxels (white) can be seen to overlap or touch one another while individual crystal centers (grey) are entirely separate. (b) Binarised final fabric of the same slice. (c) & (d) show examples of layered crystal structures of two sizes used in the algorithm (with front-right section removed to show internal layered structure).

Figure 4 Example data from sensitivity tests calculating solid volume loss due to crystal overlap. (a) Sensitivity test data and resultant trend for 400^3 models at a resolution of 0.40μm^3/voxel over a range of porosities. Using the trend it is possible to calculate the model target porosity (ϕ) that should be used in order to achieve any particular required final porosity (ϕ_D). The arrow shows that a target porosity of ϕ=18% should be used to obtain a final porosity ϕ_D=25%. (b) These sensitivity tests can be performed for any grid size (three examples are shown) and at any resolution.

Figure 5 Visual comparison between model fabrics and SEM images. (a) Micritic fabrics in a secondary electron SEM image of a broken chip. (b) Pseudo-3D view of model fabrics (resolution 0.10 μm^3/voxel). (c) Micritic fabrics in a binarised 2D back-scatter SEM image, image porosity is 30.6%. (d) 2D slice view of model fabrics (resolution 0.40 μm^3/voxel), image porosity of 30%. Note: the models have not tried to replicate the exact samples.

Figure 6 400x400voxel slice of models r_5 to r_1 scaled to relative physical size. All models have ~26% porosity.

Figure 7 Pore network properties of models r_1 to r_5. Key indicates the resolution of each model. (a) Pore radius distribution. (b) Euler number connectivity function.

Figure 8 (a) Porosities computed from subvolumes at each resolution. (b) Single-phase permeabilities computed from subvolumes at each resolution. (c) Porosity plotted against single-phase permeability computed for each model subvolume (unfilled symbols) and each full model volume (filled symbols).

Figure 9 Relative permeability (a-c) and capillary pressure curves (d-e) from simulations of multi-phase flow on models r_1 to r_5. Porosity is constant at approximately 26%. In a-c, water relative permeability curves are shown as solid lines, oil relative permeability curves are shown as dashed lines. WW= water wet wettability & FW= fractionally wet wettability.

Figure 10 An example 2D slice through a single realisation of models r_a through r_e with increasing porosity. Black voxels indicate pores, while white voxels indicate solid. All slices have dimensions of 400x400 voxels and a resolution of 0.40μm^3/voxel.

Figure 11 A comparison of micritic model fabrics before and after crystal rounding. (a) 100$voxel^3$ volume of rhombic crystal model r_c with 25% porosity. (b) 100$voxel^3$ of resulting rounded crystal model, s_c. (c) 100x100 voxel slice of rhombic crystal model r_c. (d) 100x100 voxel slice of resulting rounded crystal model, s_c. (e) Crystal diameter histogram and cumulative frequency plots for a 400x400 voxel slice of the rhombic and rounded models.

Figure 12 Pore network properties of rhombic micrite models and rounded micrite models. Upper row shows pore radius distributions and lower row shows Euler number connectivity functions. Left hand column shows results for rhombic models, central column shows results for rounded micrite models, and right hand figures show a comparison between the results for 25.6% porosity rhombic micrite (model r_c) and its resultant 33.7% porosity rounded micrite fabric counterpart (model s_c). Keys shown apply to figures directly above them.

Figure 13 Porosity against single-phase permeability for models r_a to r_e and s_a to s_e. (a) Rhombic crystal model results plotted with data from Fullmer et al (2014) and the Class III porosity-permeability trend described by Lucia (2007). Modelled fabrics represent those termed Type I by Fullmer et al (2014). Rhombic model data points represent an average porosity-permeability over three realisations. (b) Comparison between rhombic crystal and rounded crystal porosity-permeability results. Dashed lines trace the transition of the porosity-permeability measurement from the original, rhombic crystal model to its rounded counterpart. Arrows indicate a rhombic crystal model (r_d) and a rounded crystal model (s_b) with similar porosities (~30%).

Figure 14 Relative permeability curves from simulations of multi-phase flow on extracted pore networks. Upper row shows results for rhombic crystal models, lower row shows results for rounded crystal models. Water relative permeability curves are shown as solid lines, oil relative permeability curves are shown as dashed lines.

Figure 15 Capillary pressure curves from simulation of multi-phase flow on extracted pore networks from rhombic crystal models r_a to r_e (upper row) and rounded micrite models s_a to s_e (lower row).

Figure 16 Moldic mesopore models. (a) to (e) show the synthetic moldic mesopore configurations used for models M10 to M45 respectively. (f) Shows a slice through model M30 as indicated by the dashed line in (c) after the mesopores have been combined with 25% matrix porosity model.

Figure 17 Coordination number data for mesopore models with varying matrix porosity. (a) Average coordination number. (b) Maximum coordination number.

Figure 18 Porosity and single-phase permeability plots for moldic mesopore models. Shading applies to all plots; darker indicates higher matrix porosity. (a) Matrix microporosity as a proportion of total porosity. (b) Mesopore radius against single-phase permeability. The 0μm radius mesopore (x-axis) data points indicate purely micritic matrix. Boxes highlight the decrease in range of permeabilities as mesopore radius increases. At 45μm radius, the mesopores are directly connected. (c) Total porosity against permeability with trend lines linking models with the same matrix porosity and mesopores up to 30μm in diameter.

Figure 19 Multi-phase flow relative permeability curves for models M0 to M45 with varying mesopore radii (see key) and varying matrix porosity. Upper, middle and lower rows indicate models of 18%, 25% and 35% matrix porosity respectively. Arrows indicate direction of increasing mesopore radius for the oil relative permeabilities (dashed lines). Water relative permeabilities are indicated as solid lines. Boxes in (g) indicate fast water drainage in comparison to the slower drainage through steeper curve gradients either side.

Figure 20 Capillary pressure curves for models M0 to M45 with varying mesopore radii (see key) and varying matrix porosity. Upper, middle, lower rows indicate models of 18%, 25% and 35% matrix porosity respectively. Arrows indicate direction of increasing mesopore radius.

Figure 21 Plots of mesopore radius against residual oil saturation for (a) water wet imbibition and (b) fractionally wet imbibition, under varying matrix porosity. The

direction of arrows indicates direction of decreasing proportion of micropores.

Table 1 Computational properties of models r_1 to r_5. Model porosity is constant at approximately 26%.

Table 2 Crystal fabric and pore network properties of models r_1 to r_5.

Table 3 Pore network statistics for rhombic and rounded crystal models. Model name prefix represents fabric (r for rhombic, s for spherical) and suffix represents matrix porosity and links the original rhombic fabric to its resulting rounded fabric counterpart.

Table 4 Moldic mesopore model names and corresponding radius and separation distance properties.

Model Name	Resolution (μm^3/voxel)	Full Model Physical Size (μm^3)	Subvolume Model Size (voxels)
r_1	0.10	40^3	---
r_2	0.20	80^3	200^3
r_3	0.30	120^3	133^3
r_4	0.40	160^3	100^3
r_5	0.50	200^3	80^3

Model Name	Minimum Crystal Diameter (μm)	No. Crystals	Porosity (%)	Average Pore Radius (μm)	No. Nodes	No. Bonds
r_1	0.30	6417	26.9	0.26	10491	19270
r_2	0.60	39858	26.2	0.30	68037	133954
r_3	0.90	116407	26.2	0.37	141547	283997
r_4	1.20	271875	25.8	0.38	342223	709514
r_5	1.50	495190	26.0	0.44	187095	584850

	Model Name	Porosity (%)	No. Nodes	No. Bonds	No. Elements	Average Coordination No.	Average Pore Radius (μm)
Rhombic	r_a	18.9	303255	576183	879438	3.78	0.37
	r_b	21.3	323128	633370	956498	3.91	0.39
	r_c	25.6	332709	683879	1016588	4.09	0.43
	r_d	30.6	309397	663326	972723	4.27	0.48
	r_e	35.7	268670	594955	863625	4.41	0.56
Rounded	s_a	27.1	293660	623913	917573	4.23	0.47
	s_b	29.6	282337	608558	890895	4.29	0.50
	s_c	33.7	249887	547965	797852	4.36	0.56
	s_d	38.3	207306	460690	667996	4.42	0.63
	s_e	42.9	165973	369289	535262	4.42	0.71

Model Name	Mesopore Radius (μm)	Minimum Separation (voxels)
M10	10	150
M20	20	100
M30	30	50
M40	40	1
M45	45	0

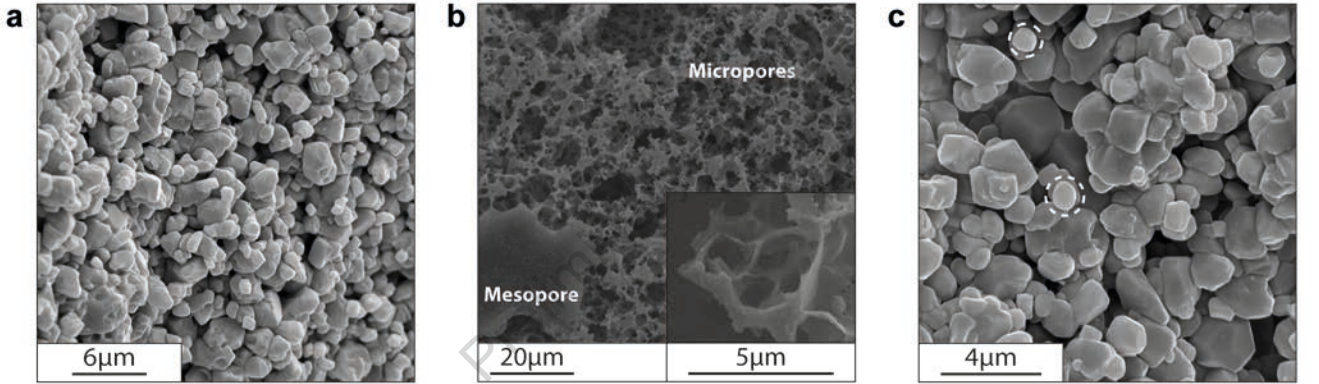
a
6μm
b
Micropores
Mesopore
20μm
5μm
c
4μm

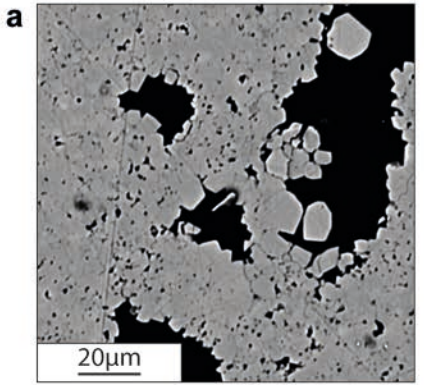
a
20μm

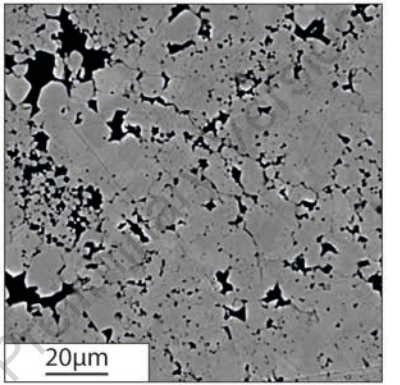
b
20μm

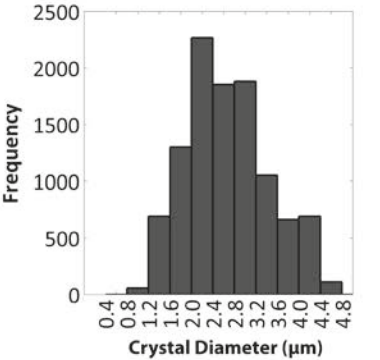
c
Frequency
2500
2000
1500
1000
500
0
0.4
0.8
1.2
1.6
2.0
2.4
2.8
3.2
3.6
4.0
4.4
4.8
Crystal Diameter (μm)

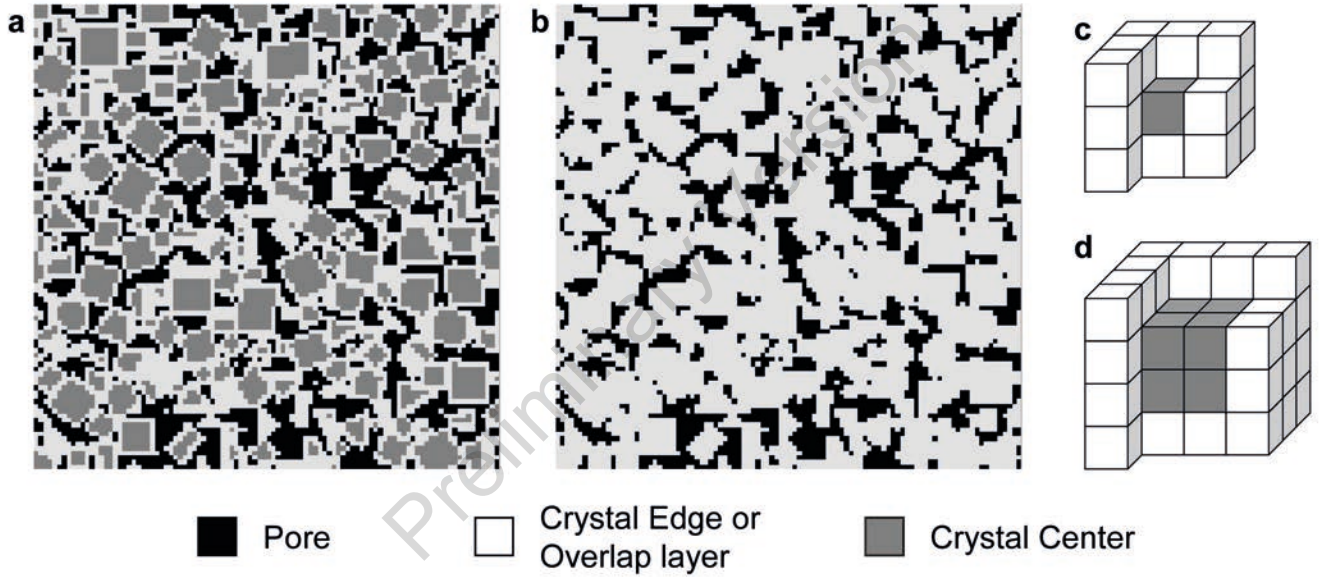

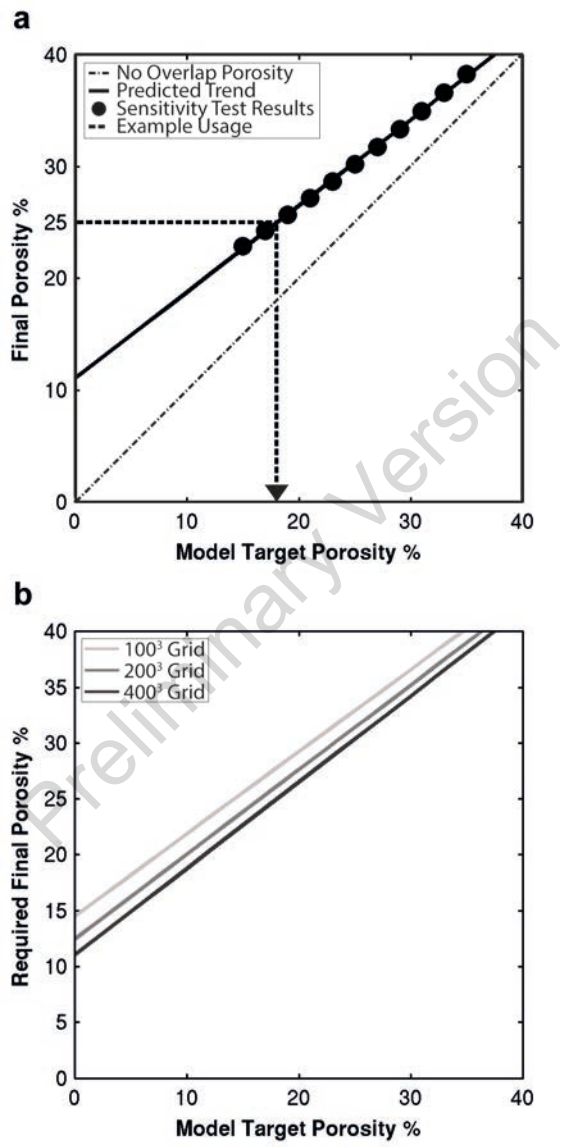

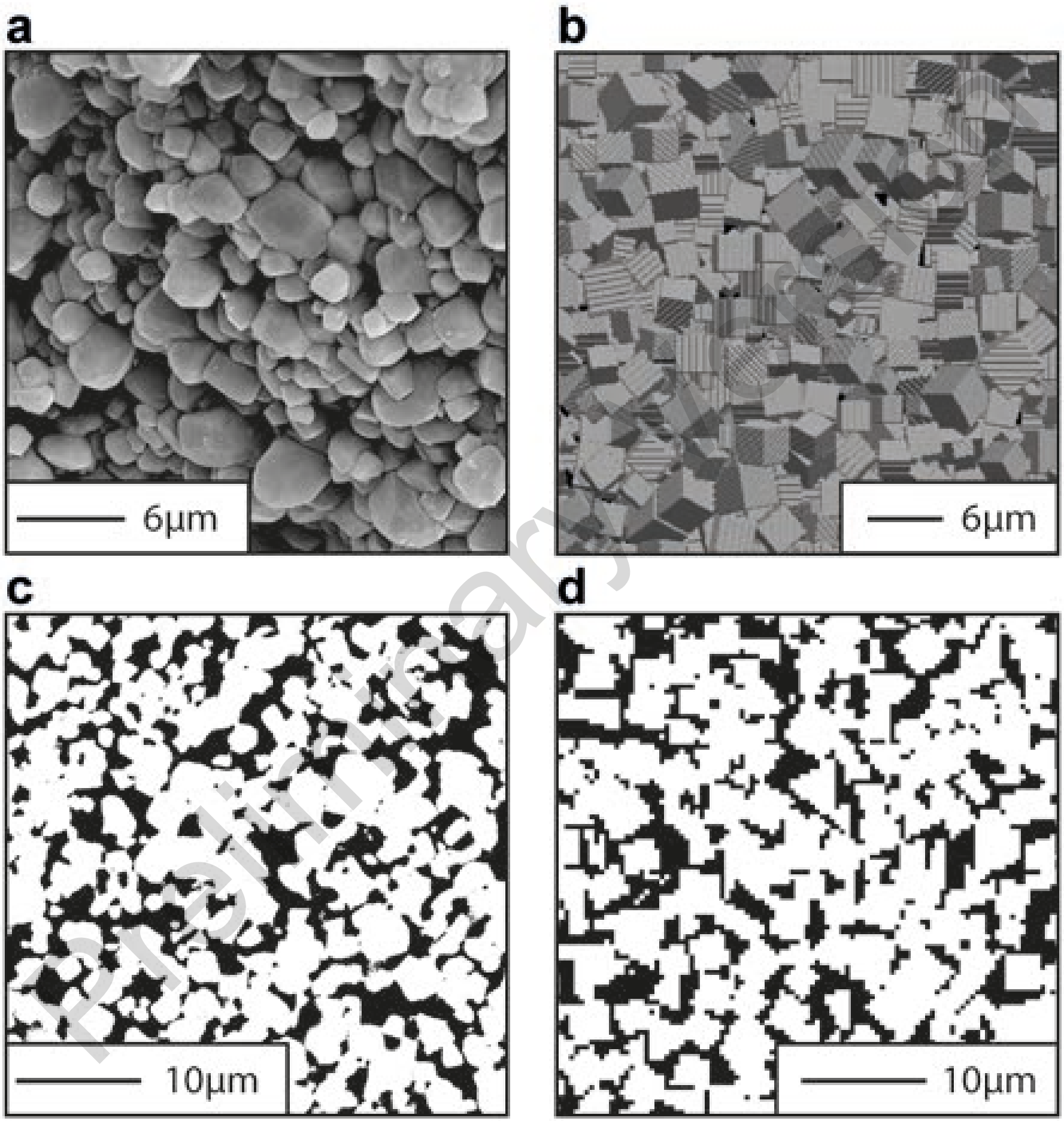

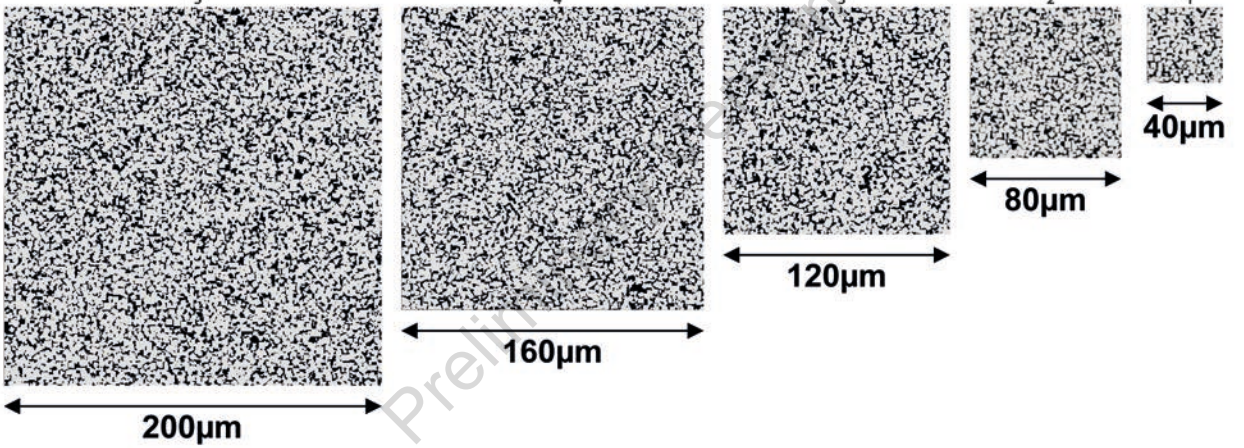
r5
r4
r3
r2
r1
40µm
80µm
120µm
160µm
200µm

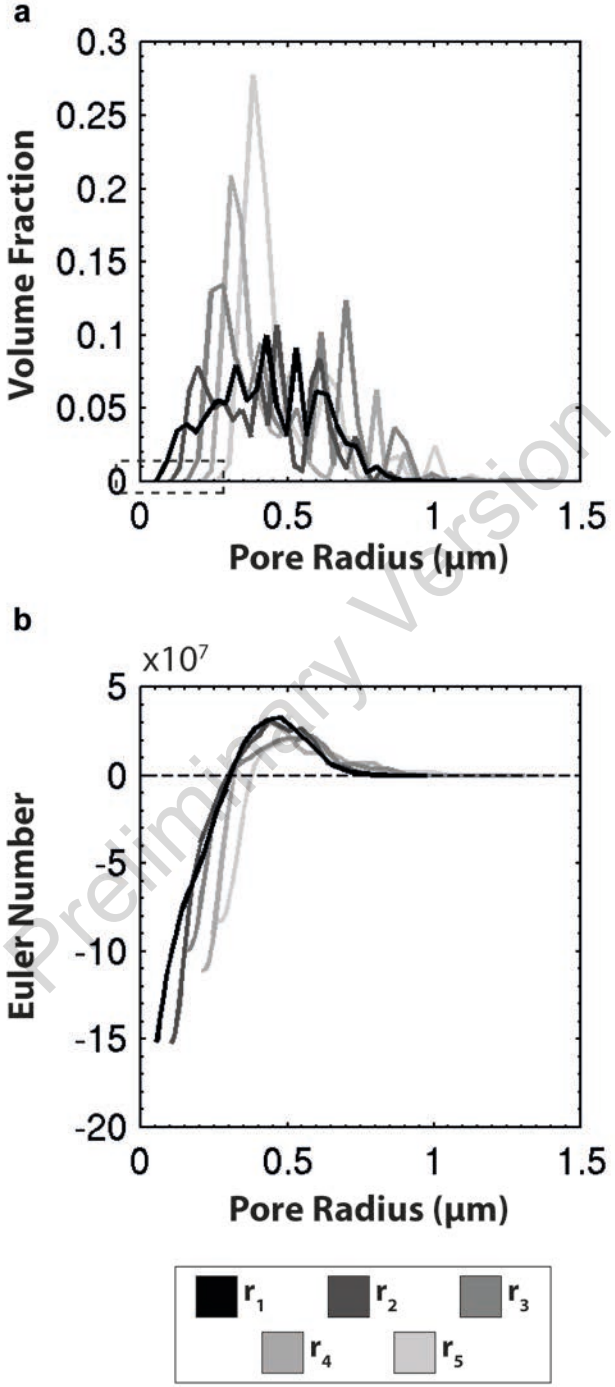

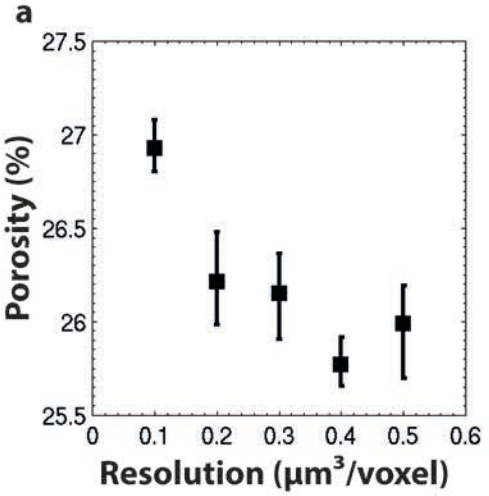

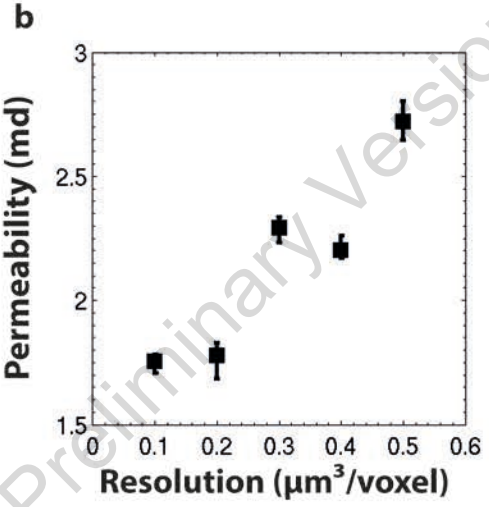

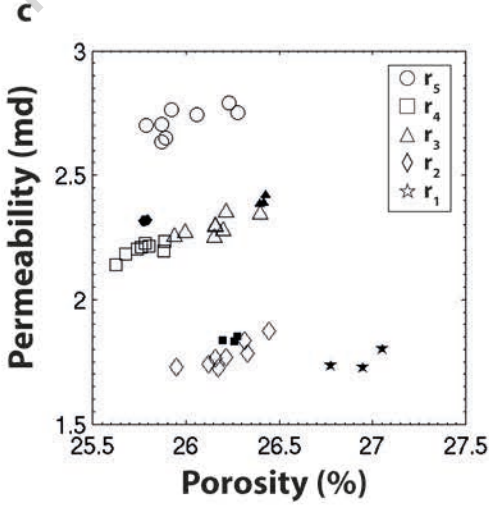

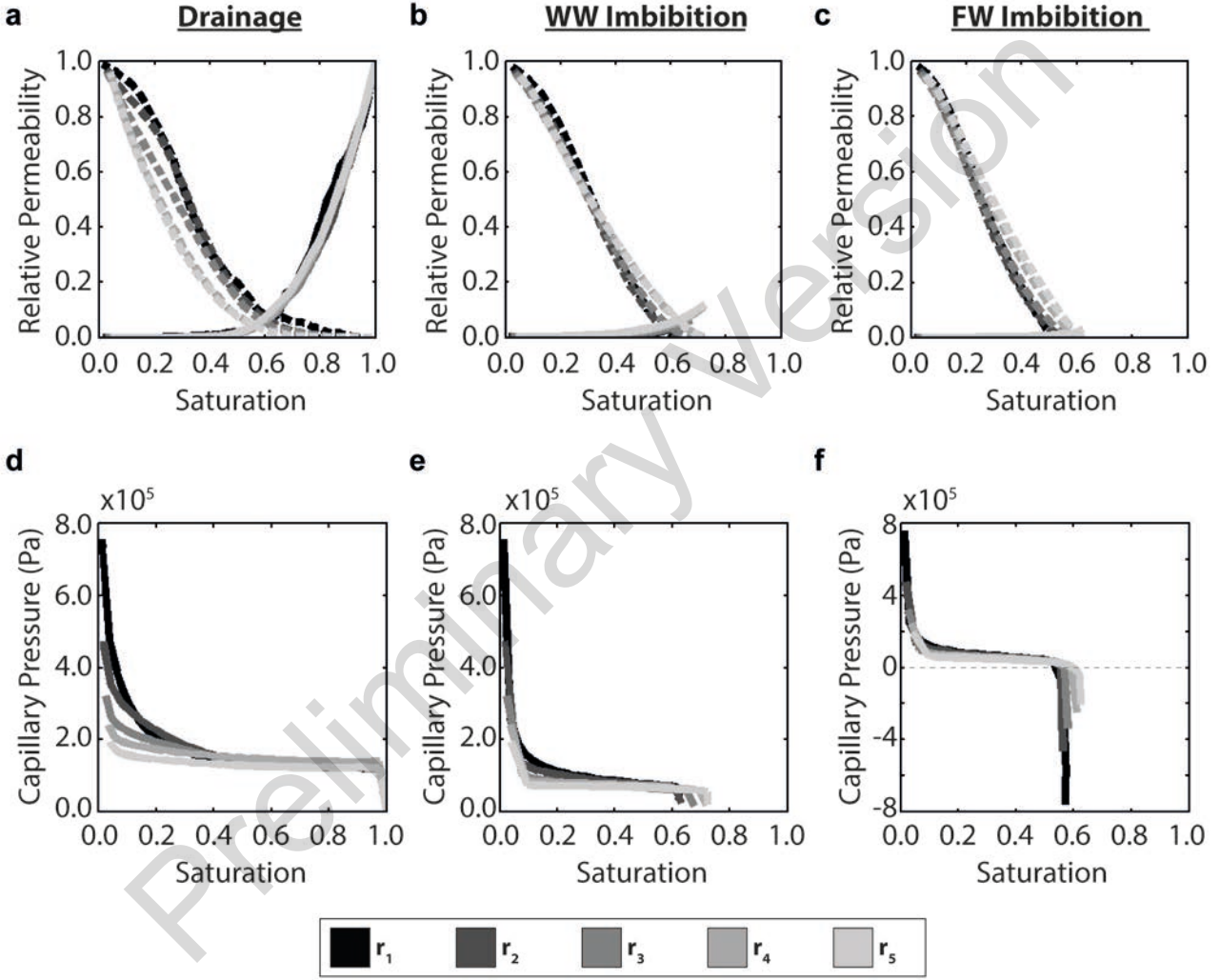

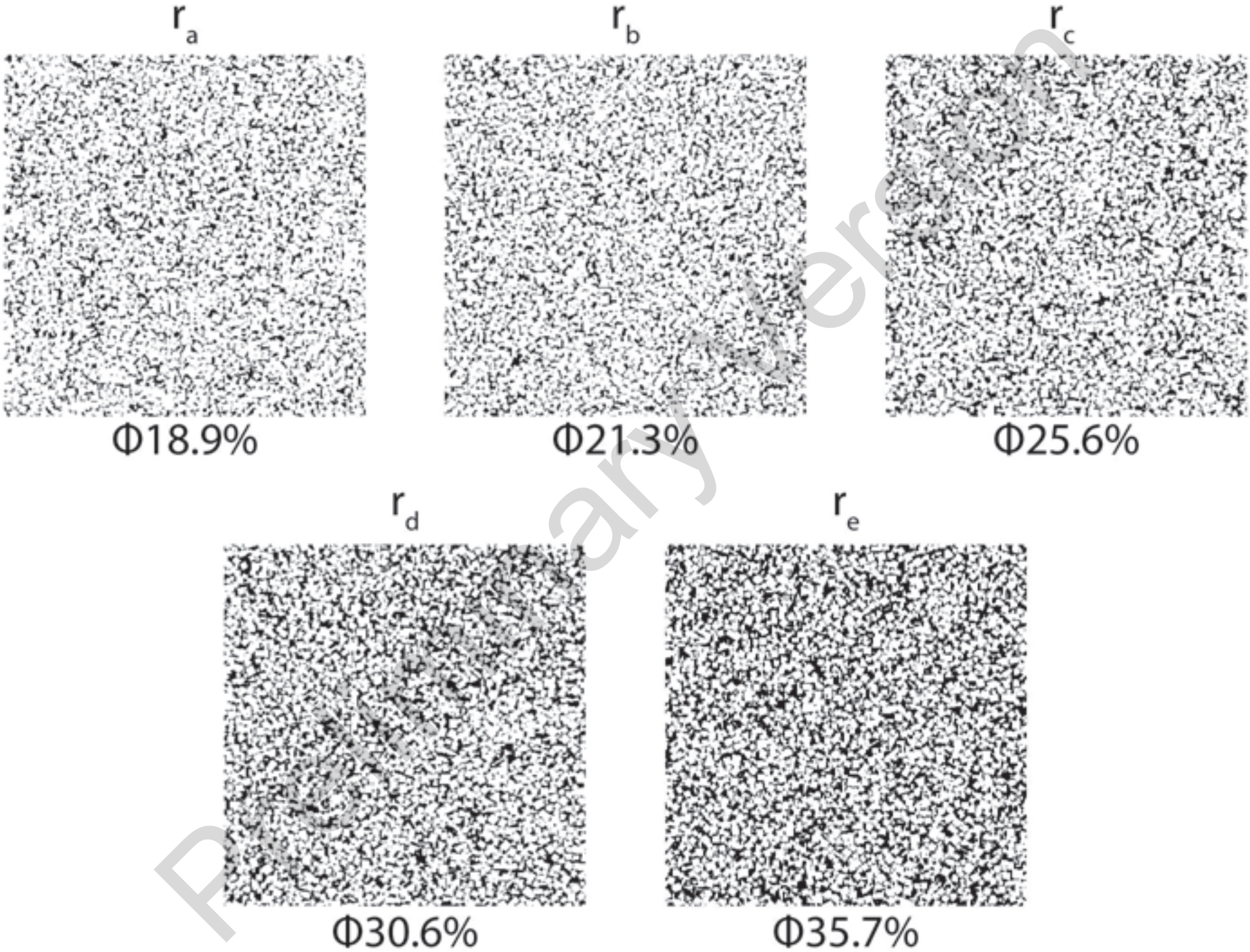
r_a
r_b
r_c
Φ18.9%
Φ21.3%
Φ25.6%
r_d
r_e
Φ30.6%
Φ35.7%

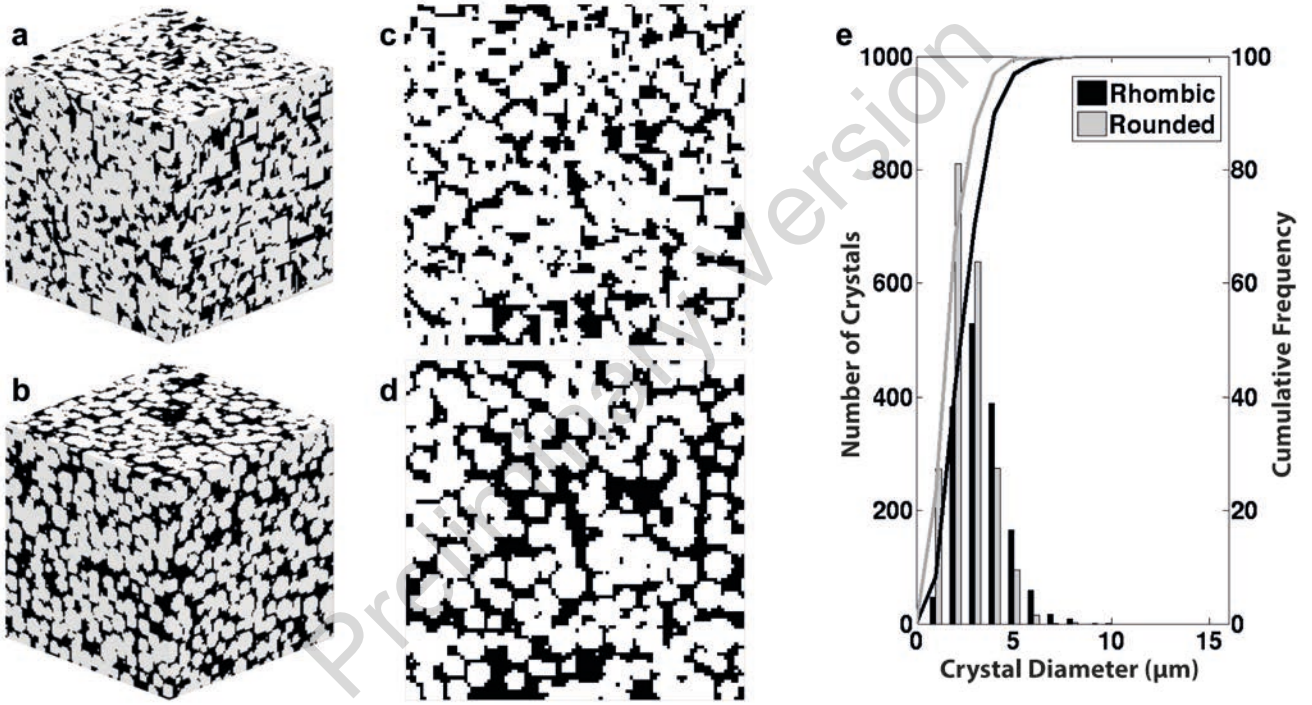

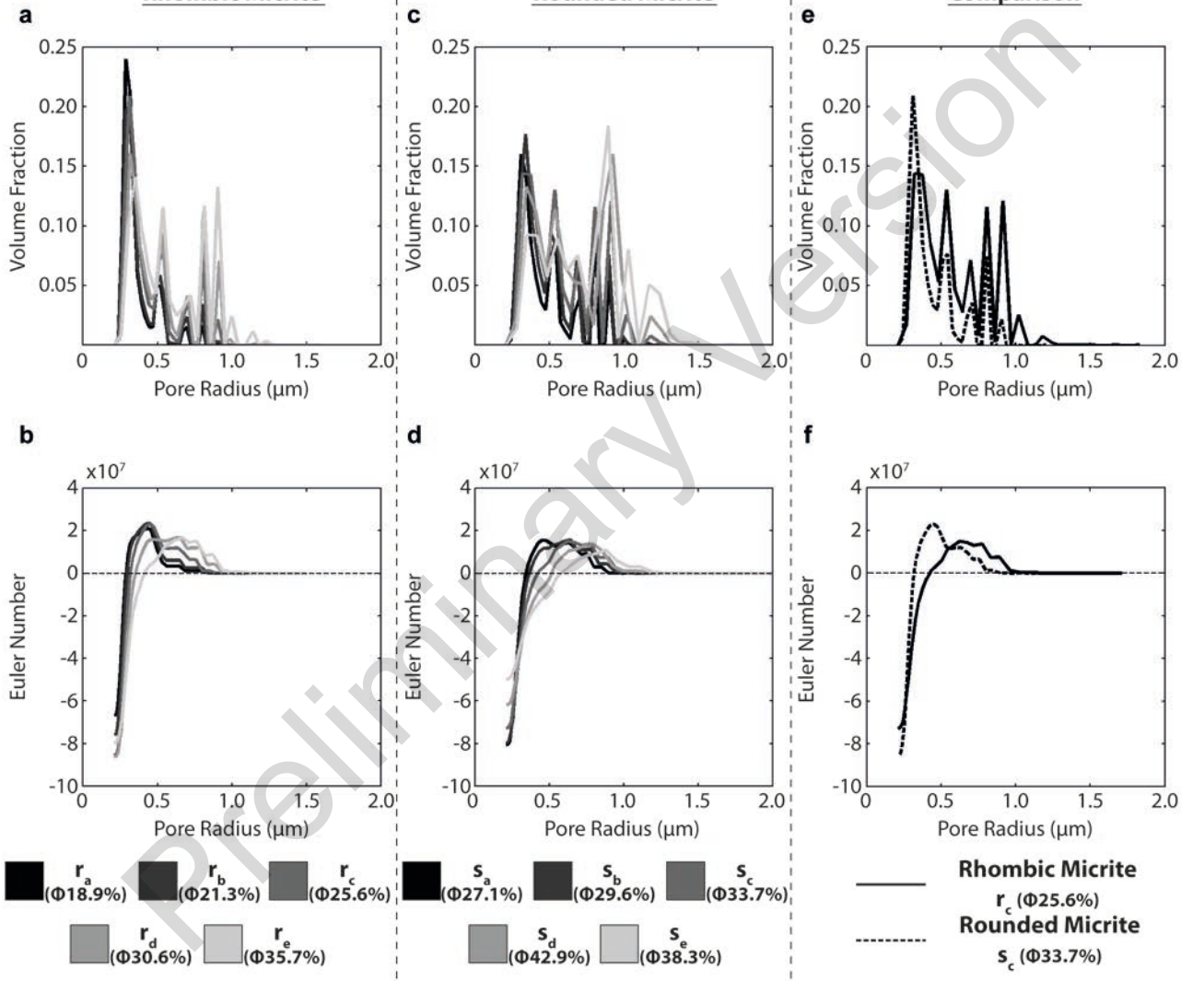

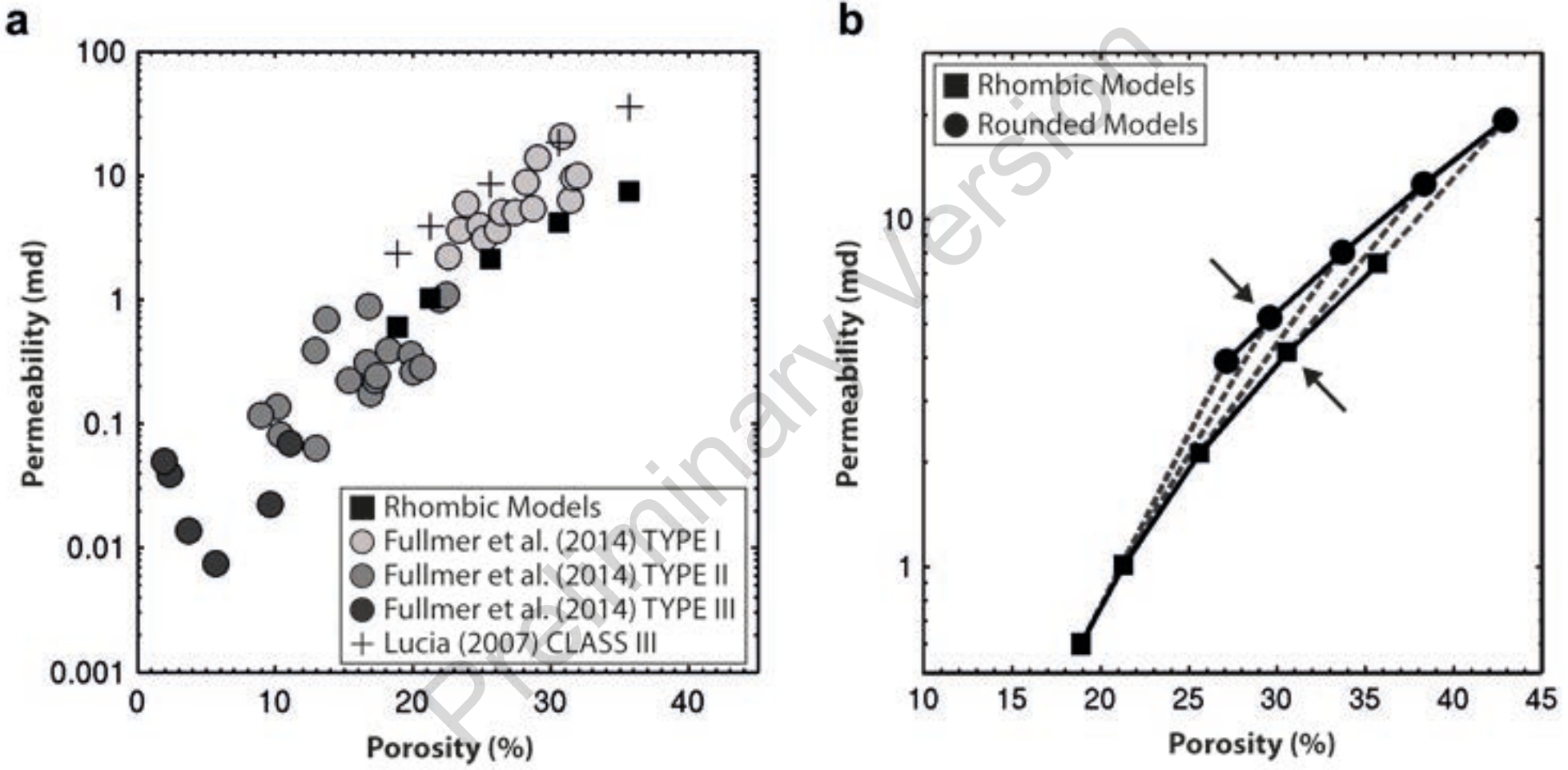

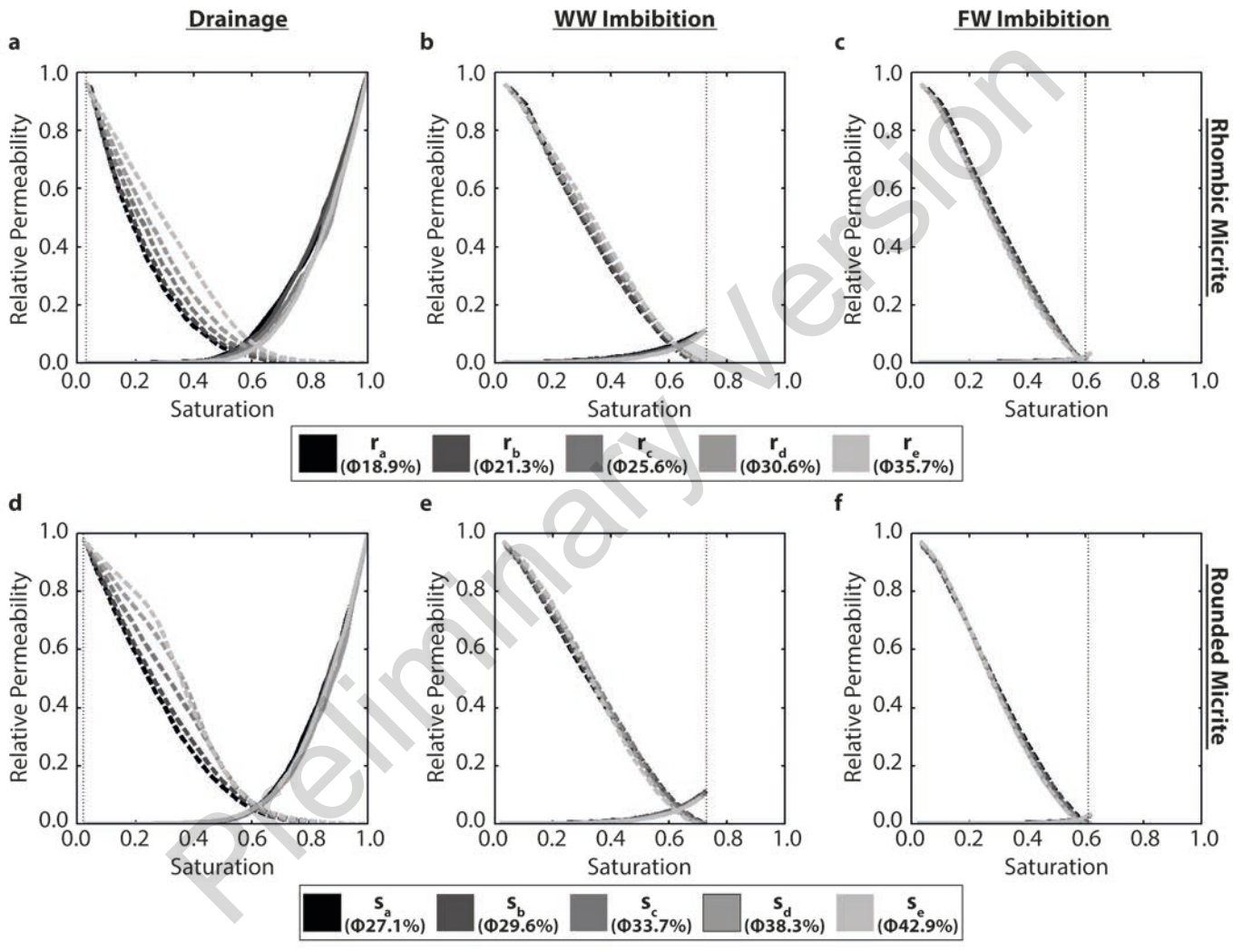

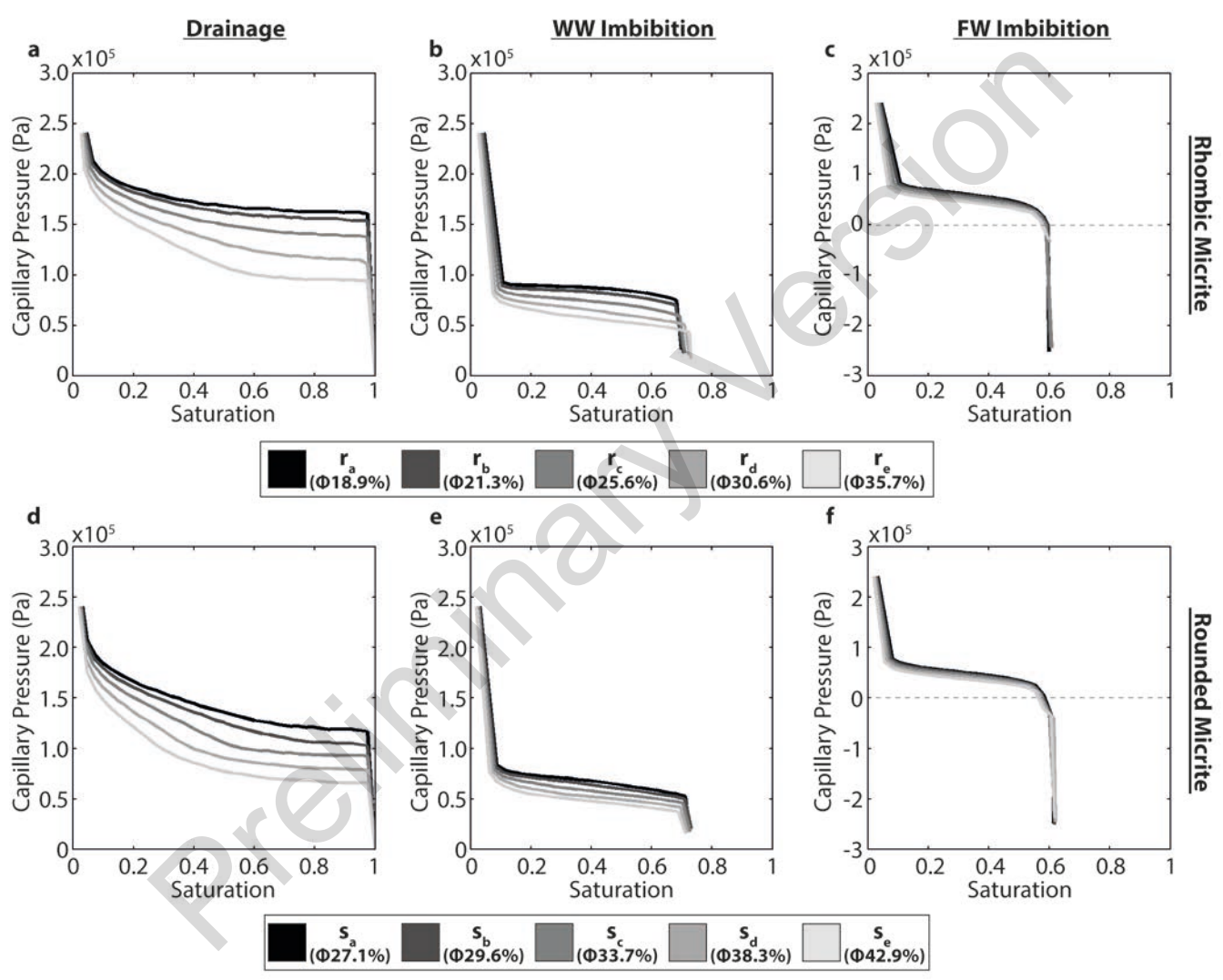

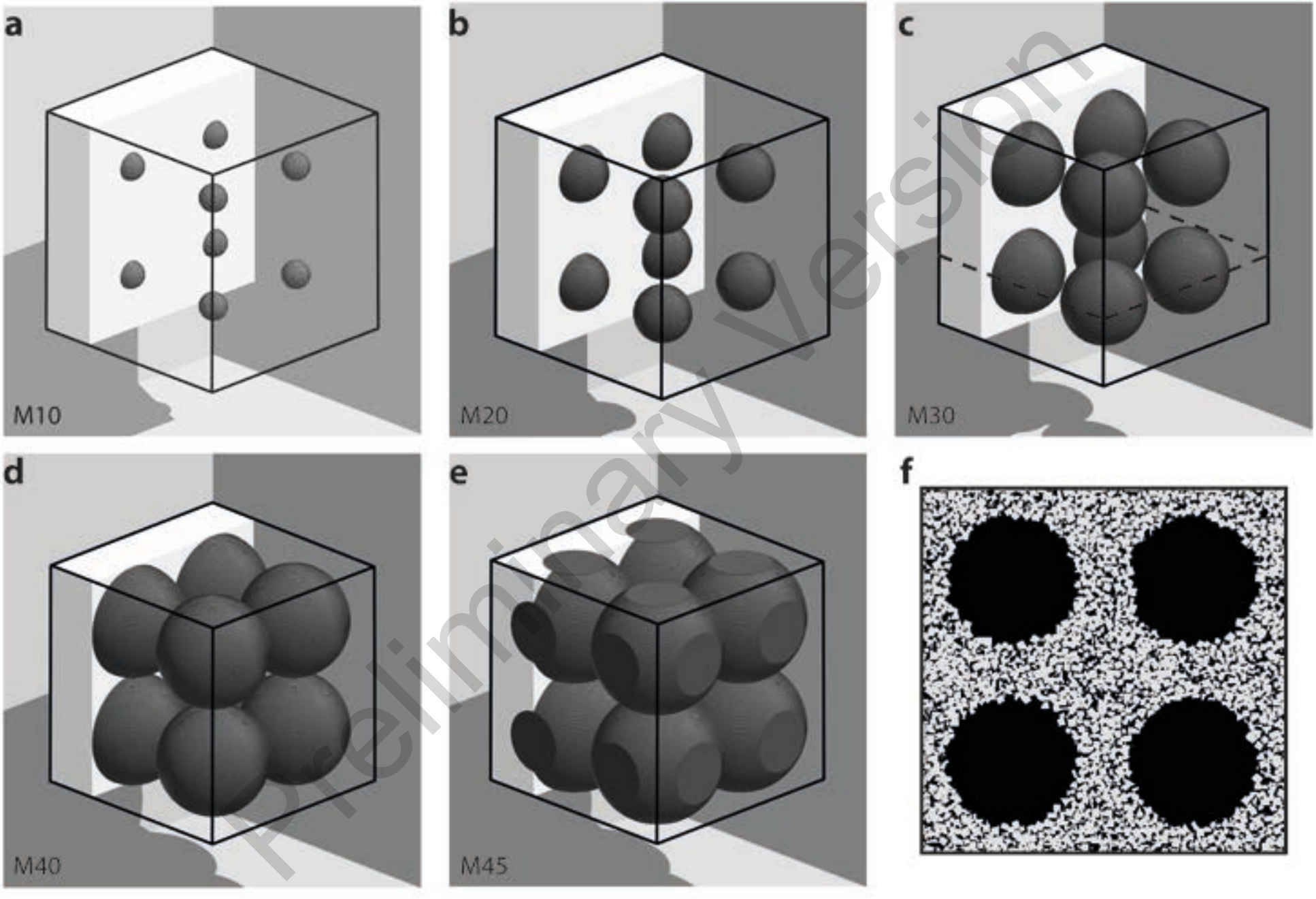

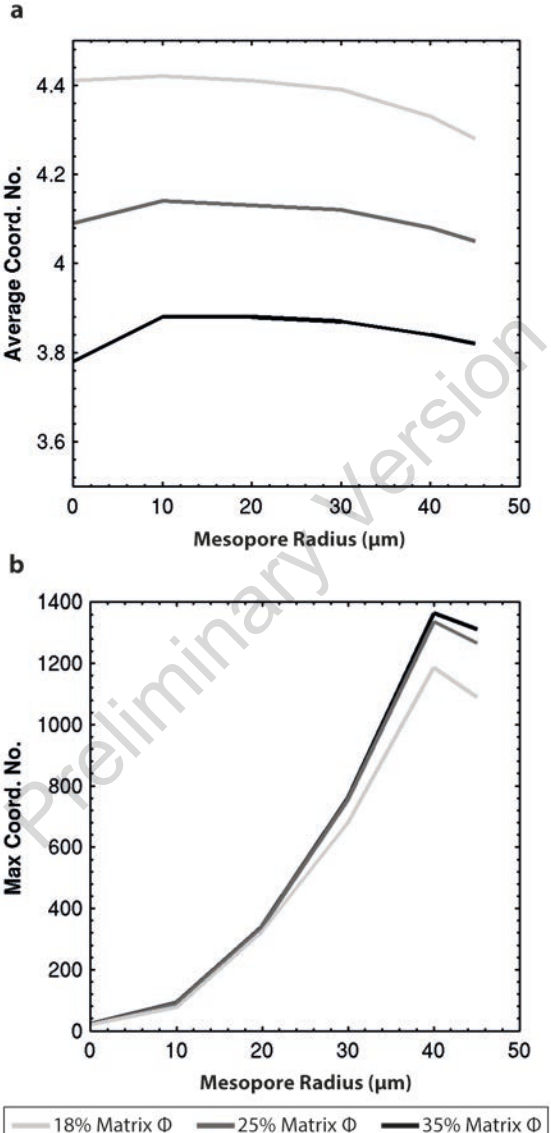

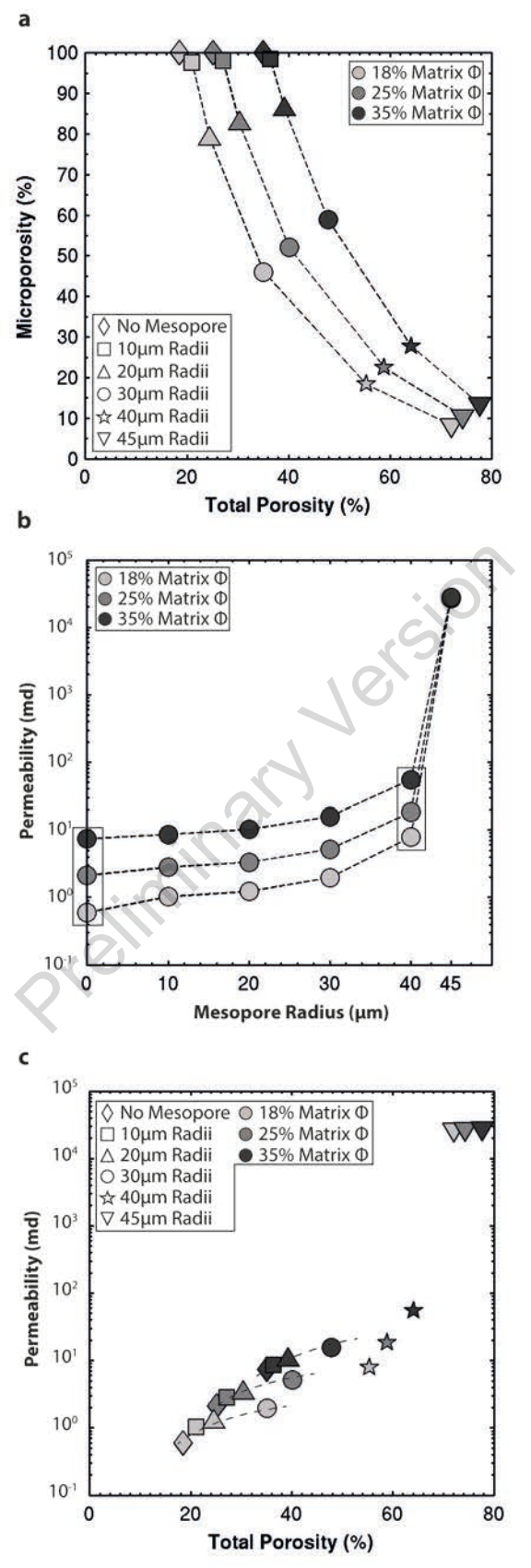

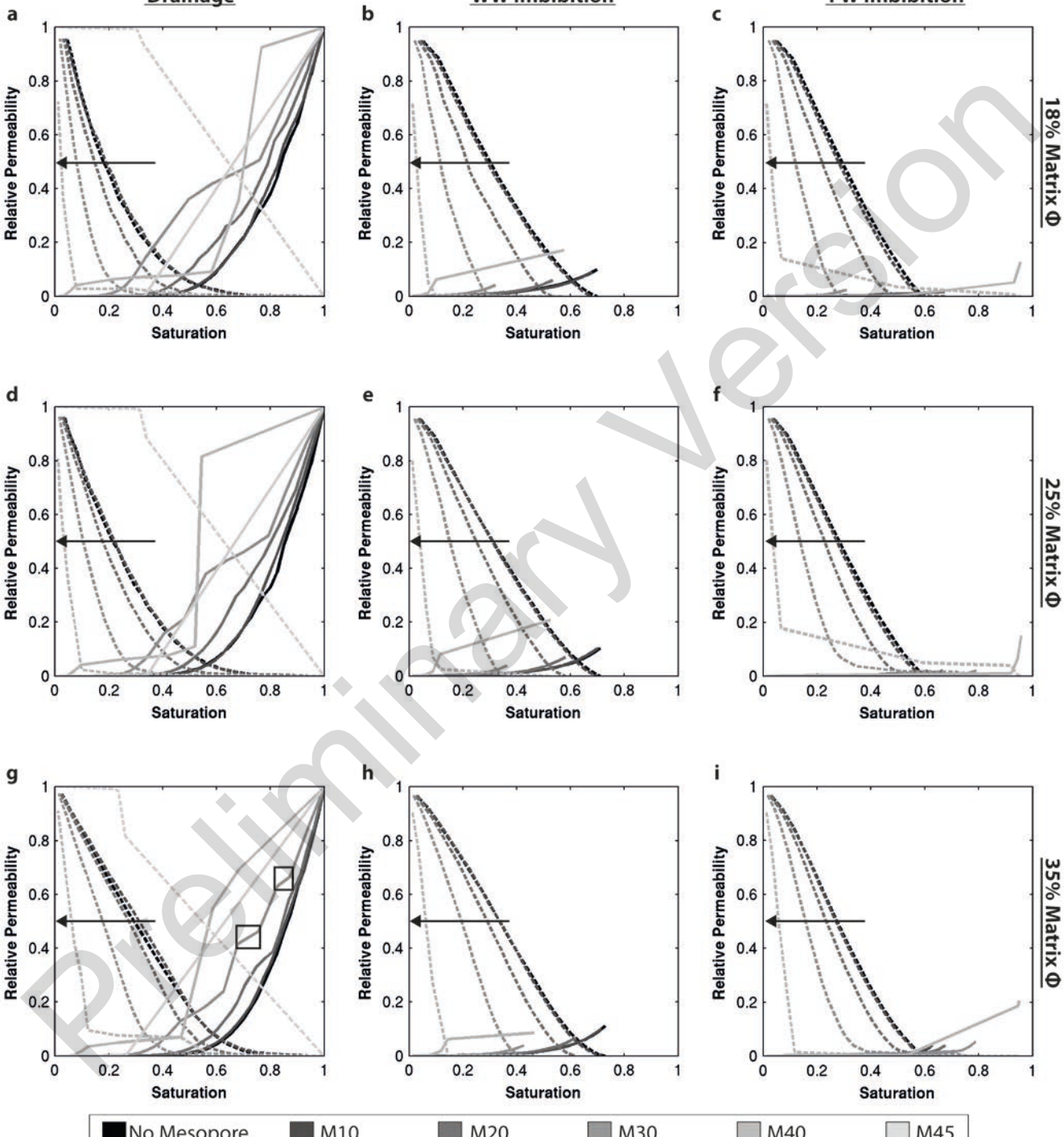

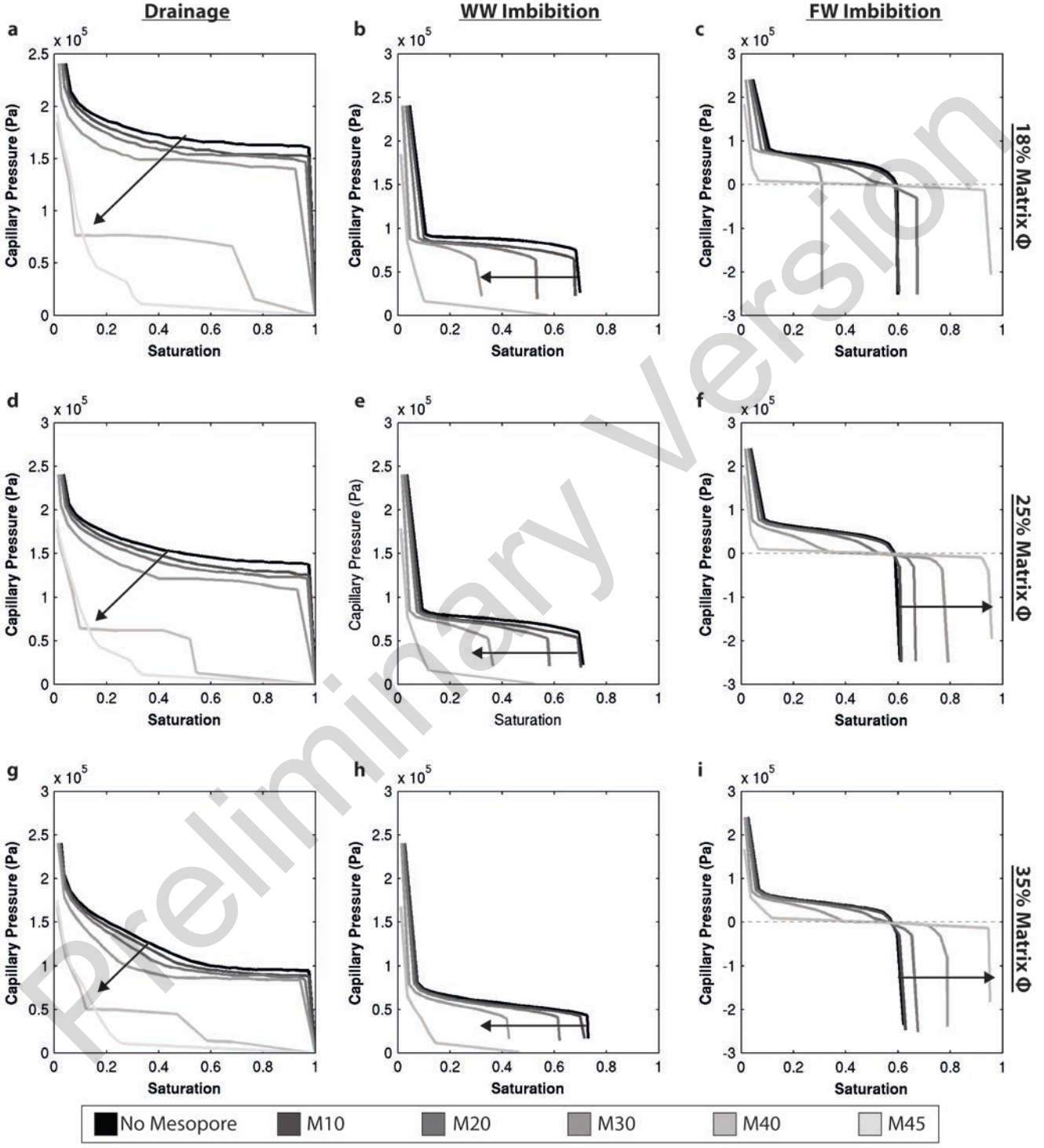

a

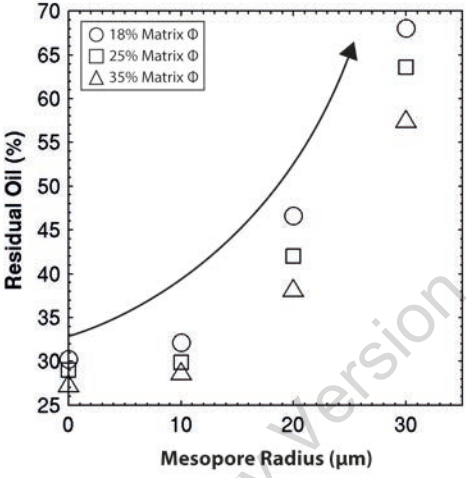

b

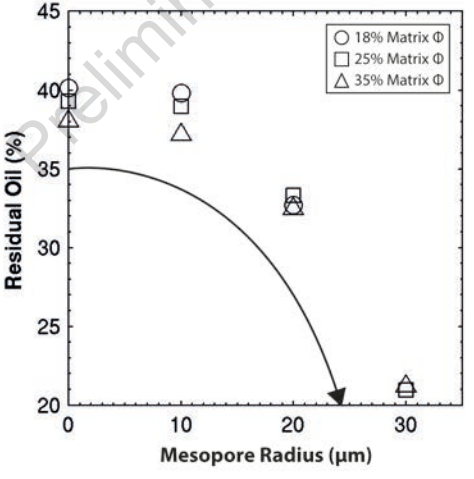

AAPG BULLETIN

Quantifying flow in variably wet microporous carbonates using object-based geological modelling and both lattice-Boltzmann and pore network fluid flow simulations

S. R. Harland, R. A. Wood, A. Curtis, M. I. J. van Dijke, K. Stratford, Z. Jiang, W. Kallel, and K. Sorbie

AAPG Bulletin published online 06 August 2015
doi: 10.1306/04231514122

Cite as: Harland, S. R., R. A. Wood, A. Curtis, M. I. J. van Dijke, K. Stratford, Z. Jiang, W. Kallel, and K. Sorbie, Quantifying flow in variably wet microporous carbonates using object-based geological modelling and both lattice-Boltzmann and pore network fluid flow simulations, *(in press; preliminary version published online Ahead of Print* 06 August 2015*):* AAPG Bulletin, doi: 10.1306/04231514122.